PAPER • OPEN ACCESS

Multi-diagnostics reconstruction of magnetic equilibrium and kinetic profiles using physics-informed neural networks with applications to JET

To cite this article: Novella Rutigliano *et al* 2026 *Nucl. Fusion* **66** 046006

OPEN ACCESS
IOP Publishing | International Atomic Energy Agency
Nuclear Fusion
Nucl. Fusion **66** (2026) 046006 (29pp)
https://doi.org/10.1088/1741-4326/ae4916

Multi-diagnostics reconstruction of magnetic equilibrium and kinetic profiles using physics-informed neural networks with applications to JET

Novella Rutigliano[1,*], Andrea Murari[2,3], Pasquale Gaudio[1], Michela Gelfusa[1] and Riccardo Rossi[1], on behalf of JET Contributors[a] and the EUROfusion Tokamak Exploitation Team[b]

[1] Dipartimento di Ingegneria Industriale, Università degli Studi di Roma 'Tor Vergata', Via del Politecnico 1, 00133 Rome, Italy
[2] Consorzio RFX (CNR, ENEA, INFN, Università di Padova, Acciaierie Venete SpA), Corso Stati Uniti 4, 35127 Padova, Italy
[3] Istituto per la Scienza e la Tecnologia dei Plasmi, CNR, Padova, Italy

E-mail: novella.rutigliano@uniroma2.it

Received 11 November 2025, revised 2 January 2026
Accepted for publication 23 February 2026
Published 11 March 2026

Abstract

Physics-informed neural networks (PINNs) are deep learning neural networks explicitly conceived as an alternative solver of partial differential equations with respect to standard numerical techniques. PINNs offer some unique features, such as the capability of constraining the solution with internal or external and local or integral information, allowing to take into account uncertainty of this information. They can also be constrained with incomplete physics equations, allowing the development of modelling tools. Therefore, they offer the possibility of developing a unique framework, which permits to combine physics and data. In this work, their potential has been investigated by applying them to one of the most important inverse problems in tokamaks, the plasma equilibrium reconstruction. More specifically, an advanced PINN-based equilibrium reconstruction method has been developed that combines multi-diagnostic constraints with high-fidelity physics modelling of the measurements, able to take into account both non-linearities and relativistic effects. All the relevant diagnostics have been included in the study, confirming the potential of the technology to perform also integrated data analysis. A series of numerical tests, performed with the help of the Tokalab platform, have proven the quality of the results in cases, for which the right solution is known. After this validation, the developed tools have been applied to analyse various Joint European Torus (JET) discharges, with particular attention to high performance experiments in DT. A detailed comparison with the reference inversion codes used on JET (EFIT, EFTP and EFTF) is reported

[a] See Maggi *et al* 2024 (https://doi.org/10.1088/1741-4326/ad3e16) for JET Contributors.
[b] See Joffrin *et al* 2024 (https://doi.org/10.1088/1741-4326/ad2be4) for the EUROfusion Tokamak Exploitation Team.
[*] Author to whom any correspondence should be addressed.

together with diagnostic ablation tests, confirming both the accuracy and the reliability of the approach. The obtained performances motivate various future developments such as the implementation of multi-fluid magnetohydrodynamic equations, plasma dynamics reconstruction, and acceleration schemes to reduce the computational times.

Keywords: physics-informed neural network, equilibrium reconstruction, multi-diagnostic, experimental data

(Some figures may appear in colour only in the online journal)

1. Introduction

Experimental physics and engineering are strongly dependant on measurements: it is impossible to conduct an experiment without measuring what is going on. This is particularly true for the field of science, in which this work is located (Magnetic Confinement Nuclear Fusion, MCNF) and its experimental apparatus (in the specific case, tokamaks). In tokamaks, integrating various diagnostics enhances our understanding of plasma behaviour [1–4], and the more diagnostics we interrogate, the more information we get. Of course, there are technological and experimental limits to the information one can get from an experiment. In the case of tokamaks, they can depend, for example, on the presence of electromagnetic forces, neutron fluxes, and high thermal loads, restricting the operation of most diagnostics to measure external local variables (e.g. pick-up coils (PUs) or flux loops (FLs)) or line-integrated quantities (e.g. interferometers, polarimeters, bolometers [5–8]). Internal local measurements are typically confined to a very small volume of the plasma (e.g. Thomson scattering (TS) [9, 10]).

Several problems in tokamak plasmas are inverse in nature: indeed, inferring plasma quantities from external or spatially integrated measurements constitutes an inverse problem. Some of the most important examples in tokamaks are tomography [11–15], kinetic profile reconstruction [16–20], and equilibrium reconstruction [21–29].

The core focus of this work is the so-called equilibrium reconstruction, which aims to evaluate the magnetic fields and the electron temperature and density. As an inverse problem, it relies on measurements and the compliance with the magnetohydrodynamic (MHD) equations. This problem can be formulated through a system of partial differential equations (PDEs) (the ideal steady-state one-fluid MHD equations) with known boundary conditions (measurements). Reconstructing equilibria is crucial in MCNF: from the reconstruction of current profile parameters and plasma shape [30–33], to discharge control [34, 35], and kinetic profiles [16, 19, 36].

Most standard reconstruction methodologies rely mainly or exclusively on magnetic diagnostics [37] (such as PUs, saddle loops (SLs) and FLs) but utilising only magnetic information renders the problem ill-posed [25, 28, 38–40], requiring algorithms capable of constraining the equilibrium with internal measurements. Moreover, as the inverse problem is formulated as a PDE, it is also fundamental to properly model diagnostics and to propagate the errors [41–44].

In recent years, physics-informed neural networks (PINNs) have emerged as an innovative approach in situations where standard methodologies are inadequate or inefficient [45–47]. PINNs and physics-informed deep learning have been useful in various scientific and technological applications, such as constraining predictive models for physics-guided extrapolation and regularisation, solving PDEs with a meshless approach and domain decomposition, and addressing problems with incomplete physics. Recent work has explored the applicability of PINNs in plasma physics and MCNF, including solving the Grad–Shafranov equation, inverse problems, turbulence, and transport simulations [48–53].

The potentialities of PINNs implementation for the study of tokamaks plasmas and the importance of a multi-diagnostics approach with a proper diagnostic modelling have already been discussed in other authors' articles [54, 55]. This work can so be considered as an advancement in PINNs application to plasma physics in tokamaks.

In this paper, we present the reconstruction of the equilibrium and the electron temperature and density profiles with the PINN technology. We demonstrate that the method is reliable in terms of stability and capable of filtering out outlier measurements within the dataset. To validate the proposed method, we first show results for a synthetic case (Tokalab [56], serving as a ground-truth reference) and then for JET (Joint European Torus) pulse #89724. We decided to test our algorithm with this discharge since it is a well-studied L-mode experiment [57] and presents several validated diagnostics. Additionally, the reconstruction of high-performance pulses #99948 (the best baseline shot in deuterium–tritium (D–T) in terms of duration and peak power [58, 59]) and #99950 (a hybrid 50/50 D/T type I ELMy H-mode shot [59, 60]) are presented. Moreover, a comparison with EFTF and EFTP for pulse #96996 is reported.

The paper is organised as follows: section 2 reviews the physical concepts related to equilibrium reconstruction, on which the PINN algorithm is based. It also describes the measurements used (in the case of JET) and the modelling of diagnostics (utilised in the simulation of the synthetic cases and in the learning algorithm for both the synthetic equilibrium and JET experiments). Section 3 introduces the PINN algorithm, detailing hyperparameters and architecture selections, and fully describes the loss function formulations. Section 4 presents and discusses the results and provides validation of the method. Finally, the conclusion section summarises the principal findings of the work.

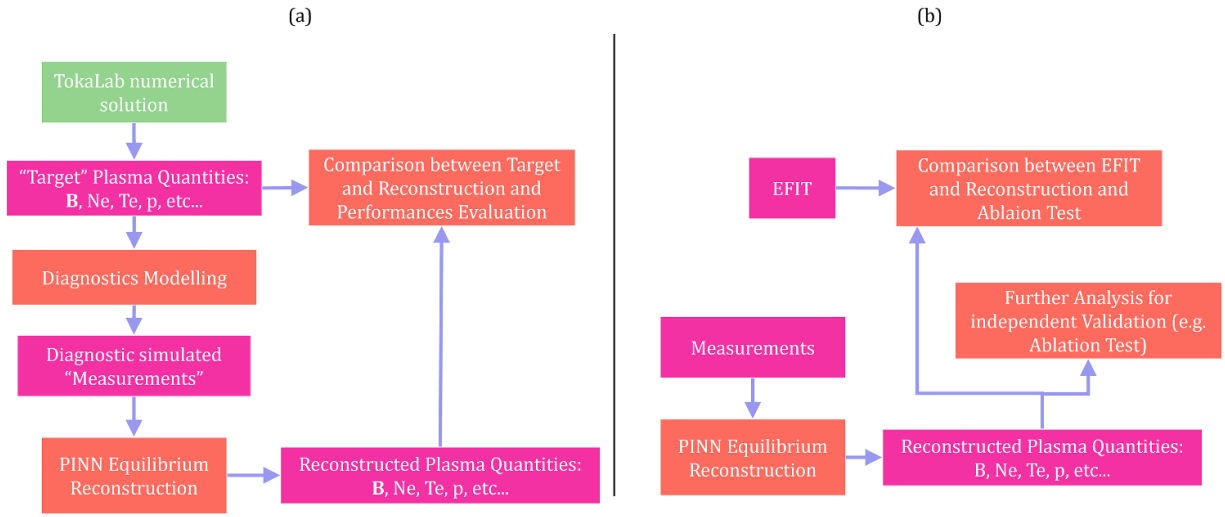

Figure 1. Schematic representation of the validation procedures followed for both synthetic (*a*) and JET experimental cases (*b*).

2. Methodology: validation schemes, data generation and diagnostics

In this section, the validation approach is introduced first and then the generation of the synthetic data and the modelling of the diagnostics are presented.

2.1. Validation methodology

Figure 1 summarises the analysis and validation procedures followed in the rest of the work for both the synthetic scenario (*a*) and JET experiments (*b*).

When analysing experimental data, the ground-truth is unknown, so, it is useful to investigate synthetic cases, to perform preliminary tests and verify the proposed method. In this work, the synthetic scenario is designed with TokaLab, an open-access virtual tokamak, which is presented in section 2.2.

Figure 1(*a*) shows the procedure followed in the first part of the work: verification and validation of the method using a scenario generated with the TokaLab case. The synthetic scenario produces the plasma quantities of interest (magnetic fields, electron density and electron temperature profiles, green box of figure 1(*a*)), from which we simulate the measurements (better described in section 2.2). The simulated measurements, together with physical equations, constitute the input to the PINN algorithm that returns, as output, the reconstructed plasma quantities of interest (bottom-right pink box). We then analyse the performances of the PINN algorithm by comparing the reconstructed quantities with the original TokaLab ones. In this way it is possible to quantify the performances of our methodology and to verify the procedure (top-right box of figure 1(*a*)). The details of the algorithm are presented in section 3.1.

For what concerns the experimental data (figure 1(*b*)), a different procedure has been used. Once again, measurements (and physical equations describing the observed phenomena) are the input to the PINN algorithm. These measurements are the ones recorded by JET diagnostics (presented in section 2.3). As output of the PINN, we obtain the plasma quantities of interest. To analyse them, since in this case the ground-truth is unknown, we made a comparison with EFIT, the standard and most established code for JET equilibrium reconstruction [30, 61, 62]. Our method aims at predicting both the magnetic fields and kinetic profiles, constraining the problem with internal and external, local and line-integrated measurements. This approach is different from the standard EFIT, which computes the equilibrium utilising only magnetic diagnostics, thus a specific validation procedure is needed. A comparison with EFTP (EFIT using internal pressure measurements) and EFTF (EFIT bounded with Faraday rotation measurements implemented assuming the type-I approximation) is also provided for pulse #96996. All the details of the validation are reported in section 4.

2.2. TokaLab geometry, equilibrium simulation and diagnostics

The synthetic scenario used as reference in the following is one of the main scenarios of TokaLab, an open access virtual tokamak for education and research [56]. Although its geometry can be readily modified, in this work, TokaLab geometrical features are fixed with the major geometrical radius $R_0 = 6$ m and the minor radius $a = 2$ m. The equilibrium has been obtained using a standard finite difference algorithm that resolves the Grad–Shafranov equation [37, 63], where the plasma boundary (last closed flux surface, LCFS) is imposed using the parametric function detailed in [64]. The equilibrium has been computed assuming a Single Null (SN) configuration, with a plasma current of 12 MA and a toroidal field of 5 T. In the numerical simulation, a pressure of 100 Pa at the LCFS is imposed.

Figure 2(*a*) shows TokaLab geometry and diagnostic set.

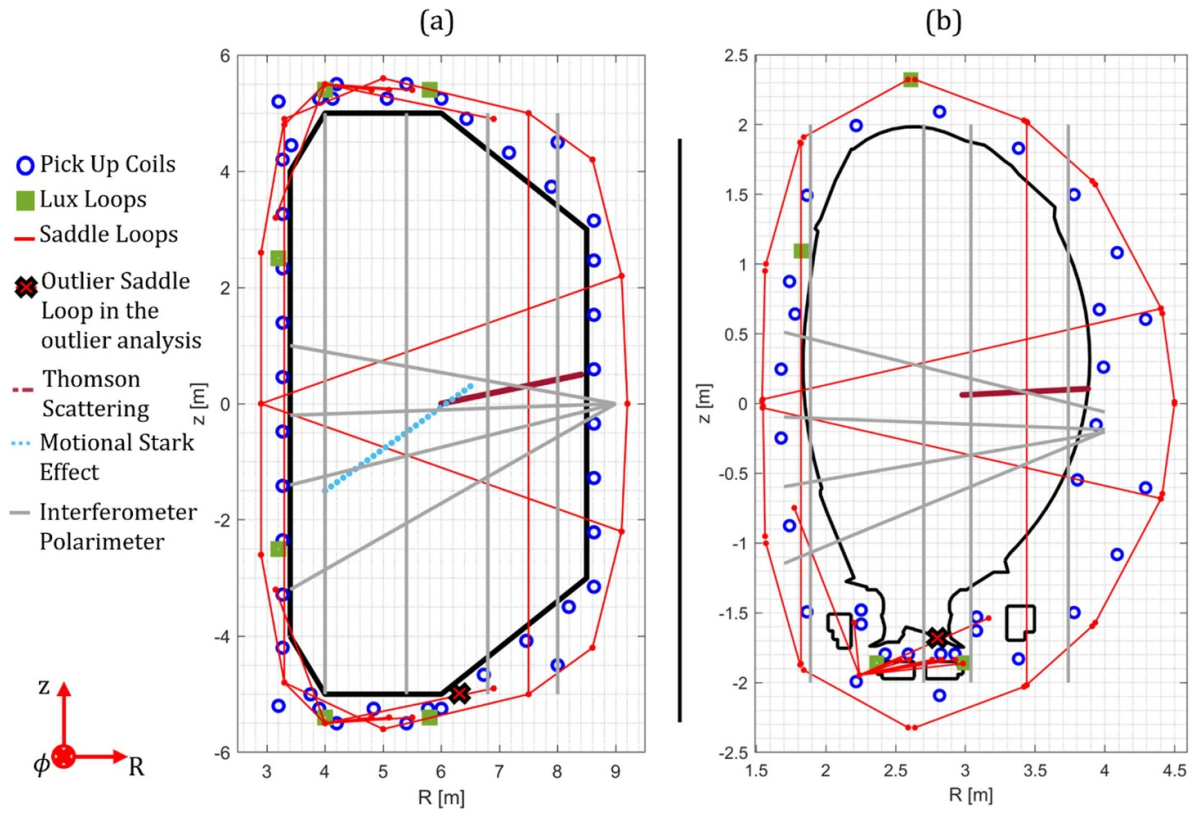

Figure 2. Geometry and diagnostic settings for TokaLab (on the left) and JET (on the right).

The physics equations used for simulating the TokaLab plasma equilibrium are introduced below. Even if in this work it is not so important to present in detail how TokaLab simulates the plasma equilibria, reporting the equations below is useful, since they are the same used for the training algorithm of the PINN and so they will be recalled later.

For simplicity's sake, the plasma equilibrium reconstruction in nuclear fusion is normally based on the ideal (no resistivity) steady-state static (negligible velocity) single-fluid MHD equations, which can be written as:

$$\begin{aligned} \nabla \cdot \boldsymbol{B} &= 0 \\ \mu_0 \boldsymbol{J} &= \nabla \times \boldsymbol{B} \\ \boldsymbol{J} \times \boldsymbol{B} &= \nabla p \end{aligned} \tag{1}$$

where $\boldsymbol{J}$ is the plasma current density, $\boldsymbol{B}$ is the magnetic field, and p is the plasma pressure. The equilibrium reconstruction is an inverse problem aiming at reconstructing the magnetic fields, plasma density currents and pressure.

The MHD equations in tokamaks are typically expressed in cylindrical coordinates (R, ϕ, z) and toroidal symmetry ($\partial/\partial\phi = 0$) is assumed. Under these hypotheses, the MHD scalar form is:

$$\nabla \cdot \boldsymbol{B} = 0 \rightarrow \frac{\partial B_R}{\partial R} + \frac{\partial B_z}{\partial z} = 0$$

$$\mu_0 \boldsymbol{J} = \nabla \times \boldsymbol{B} \rightarrow \begin{bmatrix} J_R = -\frac{1}{\mu_0}\frac{\partial B_\phi}{\partial z} \\ J_\phi = \frac{1}{\mu_0}\left(\frac{\partial B_R}{\partial z} - \frac{\partial B_z}{\partial R}\right) \\ J_z = \frac{1}{\mu_0}\left(\frac{B_\phi}{R} + \frac{\partial B_\phi}{\partial R}\right) \end{bmatrix}$$

$$\boldsymbol{J} \times \boldsymbol{B} = \nabla p \rightarrow \begin{bmatrix} J_\phi B_z - J_z B_\phi = \frac{\partial p}{\partial R} \\ J_R B_z - J_z B_R = 0 \\ J_R B_\phi - J_\phi B_z = \frac{\partial p}{\partial z} \end{bmatrix}. \tag{2}$$

It is possible to manipulate them to write the Grad–Shafranov equation:

$$\Delta^* \Psi = -\mu_0 (2\pi R)^2 \frac{\mathrm{d}p}{\mathrm{d}\Psi} - (2\pi)^2 F \cdot \frac{\mathrm{d}F}{\mathrm{d}\Psi} \tag{3}$$

where Ψ is the magnetic flux (Wb). In this paper the normalised flux per unit radiant ψ (Wb rad^{-1}) is also used.

In this study, we have implemented the approximation that electron and ion densities are equal ($N_e = N_i = N$) and that electron and ion temperatures are equal ($T_e = T_i = T$). Under this approximation, the plasma pressure is $p = 2NT$. The electron density is subsequently calculated using a typical radial

function on the normalised flux surface (ψ_n):

$$N_e(\psi_n) = (N_{e,0} - N_{e,\mathrm{LCFS}})(1 - \psi_n^{\alpha_1})^{\alpha_2} + N_{e,\mathrm{LCFS}} \quad (4)$$

where $N_{e,0}$ is the electron density on the magnetic axis while $N_{e,\mathrm{LCFS}}$ is the density on the LCFS. It follows that the temperature is equal to:

$$T_e = \frac{p}{2eN_e}. \quad (5)$$

Once all the synthetic plasma quantities are computed, it is possible to model the diagnostics and, so, to simulate the measurements.

Regarding the diagnostics, the second part of this Subsection introduces the modelling procedures adopted to simulate the measurements in TokaLab. Once again, the formulation introduced here will be recalled later because, as a part of the PINN training algorithm, the diagnostic measurements will be calculated from the reconstructed plasma quantities, following the same procedure adopted for the TokaLab simulations.

For the TokaLab case, the diagnostics modelled are shown in figure 2(*a*) and include PUs, FLs, SLs, TS, interferometer-polarimeter (IP), and the motional Stark effect (MSE). Each diagnostic includes multiple measurements; for instance, the interferometer has 8 lines of sight. In the following, the index '*i*' denotes each individual measurement.

The PUs, which are induction sensors, measure the local magnetic field along the coil axis direction (n), which forms an angle γ with the poloidal surface axis, with each measurement calculated as [2, 65]:

$$B_{\mathrm{PU}i} = B(R_i, z_i) \cdot n(Ri, zi) = B_R(R_i, z_i)\cos(\gamma_i) + B_z(R_i, z_i)\sin(\gamma_i) \quad (6)$$

where R_i and z_i are the coordinates of the coil centre.

FLs and SLs measure the magnetic field linked to the loop, expressed as:

$$\psi_{\mathrm{FL}i} = \psi(R_i, z_i) \quad (7)$$

$$\psi_{\mathrm{SL}i} = \psi(R_2, z_2) - \psi(R_1, z_1) \quad (8)$$

where the subscripts 1 and 2 indicate the extremities of the SLs, considering a counterclockwise orientation.

TS, a laser-based diagnostic, evaluates the local electron density and temperature at various points by analysing the laser light scattered by the plasma [2]:

$$Ne_{\mathrm{TS}i} = N_e(Ri, zi)$$
$$Te_{\mathrm{TS}i} = T_e(Ri, zi). \quad (9)$$

The IP is used to measure the line-integrated density (LID) [2]:

$$\mathrm{LID}_i = \int N_e \mathrm{d}Z \quad (10)$$

where dZ is the infinitesimal distance along the interferometer's line of sight.

For polarimetric measurements (Faraday rotation and Cotton–Mouton phase shift), we use the complete Stokes formulation [66]. Being $\mathbf{\Omega}$ a vector modelling the plasma, the Stoke's vector describing the evolution of the polarised light along the optical path is:

$$\frac{\mathrm{d}\mathbf{s}(Z)}{dZ} = \mathbf{\Omega}(Z) \times s(Z) \rightarrow \begin{cases} \mathrm{d}s_1/\mathrm{d}Z \\ \mathrm{d}s_2/\mathrm{d}Z \\ \mathrm{d}s_3/\mathrm{d}Z \end{cases} \quad (11)$$

with:

$$\mathbf{\Omega}(Z) = \begin{bmatrix} \Omega_1 \\ \Omega_2 \\ \Omega_3 \end{bmatrix} = \begin{bmatrix} C_1\lambda^3 N_e(Z)\left(B_x^2(Z) - B_y^2(Z)\right) \\ 2C_1\lambda^3 N_e(Z) B_x(Z) B_y(Z) \\ C_3\lambda^2 N_e(Z) B_z(Z) \end{bmatrix}. \quad (12)$$

From the previous equations it is possible to derive the Faraday rotation and Cotton–Mouton phase shift as follows:

$$\mathrm{Far} = \frac{1}{2}\int \Omega_3(Z)\,\mathrm{d}Z - \frac{1}{2}\int \frac{\Omega_1(Z)s_1(Z)s_3(Z) + \Omega_2(Z)s_2(Z)s_3(Z)}{s_1^2(Z) + s_2^2(Z)}\mathrm{d}Z$$
$$\mathrm{CM} = \int \Omega_1(Z)\,\mathrm{d}Z - \int \frac{\Omega_2(Z)s_2(Z)s_1(Z) + \Omega_3(Z)s_3(Z)s_1(Z)}{s_2^2(Z) + s_3^2(Z)}\mathrm{d}Z. \quad (13)$$

The derivation of this formulation is presented in [55], while the importance of using the complete formulation is discussed in [41, 55].

The MSE diagnostic is based on the measurement of the light polarisation emitted by a beam of hydrogen neutral atoms injected into the plasma [2]. Due to the motion of the ions inside the tokamak magnetic field, an apparent electric field is generated that causes the Stark effect. By measuring the light polarisation, it is possible to determine the direction θ of the magnetic field in the plasma

$$\mathrm{MSE}_i = \theta(R_i, z_i). \quad (14)$$

It is crucial to note that the algorithm's modularity allows for easy implementation of additional diagnostics (both for their simulation through TokaLab and for their implementation in the PINN multi-diagnostic algorithm).

To simulate the diagnostics realistically in the synthetic scenario, normally distributed random noise has been added to the ideal measurements. It is important to highlight that both the geometric configurations and the noise uncertainties for the TokaLab diagnostics are based on JET diagnostic configuration and statistics [8, 9, 65]. Table 1 displays the number and the set of diagnostics used for the PINN algorithm for both TokaLab scenario and all JET pulses. The measurement uncertainties are also reported.

2.3. JET geometry and diagnostics

Figure 2(*b*) shows JET geometry and diagnostic positions. As for the TokaLab case, in table 1 the number of diagnostics and the diagnostic sets used for each pulse reconstruction are reported.

Table 1. Number and set of diagnostics used in each case. (The acronymous stand for: PU = pick-up coils, FL = flux loops, SL = saddle loops, TS = Thomson scattering, LID = interferometry line integrated density, POL-Far = polarimetry-Faraday rotation, POL-CM = polarimetry-Cotton–Mouton phase shift, MSE = motional Stark effect).

	Pulse	PU	FL	SL	TS	LID	POL-Far	POL-CM	MSE
Tokalab	—	42	6	30	60	8	8	8	25
	σ	σ_{PU} $= 0.05$ T	$\sigma_{\mathrm{FL}} =$ 0.05 Wb rad^{-1}	$\sigma_{\mathrm{SL}} =$ 0.05 Wb rad^{-1}	$\sigma_{\mathrm{TS}_{Ne}}$ $= 10^{18}$m^{-3} $\sigma_{\mathrm{TS}_{Te}}$ $= 100$ eV	$\sigma_{\mathrm{TS}_{Ne}}$ $= 10^{18}$m^{-3}	σ_{Far} $= 3.5$ mrad	σ_{CM} $= 3.5$ mrad	σ_{MSE} $= 1.7$ mrad
JET	89724	36	4	27	63	6 [1,3,4,6,7,8]	4 [1,2, 3,4]	—	—
	99948	36	4	27	63	5 [3,4,6,7,8]	4 [1,2,3,4]	—	—
	99950	36	4	27	63	5 [3,4,6,7,8]	6 [1,2,3,4,7,8]	—	—
	96996	36	4	27	63	6 [2,3,4,6,7,8]	8 [1,2,3,4,5,6,7,8]		

The uncertainties are calculated as the standard deviation of the measurements in the considered time window.

For JET pulses, it is important to underline that it has been necessary to operate a choice and neglect some measurements from the set of diagnostics, namely some lines of the interferometer and of the polarimeter. For what concerns the interferometer, as it can be clearly see from figure 2, line 2 intercepts the divertor and its measurements are altered by the density in the private region and the SOL. Different physical equations should be used in those regions, requiring a multi-physics approach. Regarding the Faraday rotation, sometimes the measurements of the horizontal lines are too noisy and so we decided not to use them to train the model. Unfortunately, for the considered instants of time of each pulse, the Cotton–Mouton phase shift measurements are all too noisy and not in agreement with the Faraday rotation information, so we decided not to consider at all that set of measurements.

In general, in the case of JET data, all the measurements have been averaged in a time window equal to 50 ms centred at the interested instant of time. The assumed uncertainties are equal to the maximum value between the declared errors bars from JET and the measurement standard deviation in the considered time window.

3. Equilibrium reconstruction with PINNs

Equilibrium reconstructions are based on the MHD equations, which are PDEs traditionally solved using numerical techniques such as finite volumes, finite differences, or finite elements. These techniques require the domain to be discretised, which generally affects the accuracy of the results. Partial derivatives are approximated using finite differences, where the step size depends on the element size. PINNs present an innovative method for solving PDEs [45, 67, 68].

A PINN is a deep neural network, whose training algorithm is guided by physical constraints. According to the universal approximation theorem, a deep neural network can approximate any function $F(x,\theta) = y$, where y is the target, x is the input space, and θ represents the function parameters. The training process consists of tuning the network parameters to best approximate the desired target, satisfying both data and physics constraints.

One significant advantage of PINNs is that all partial derivatives are computed using automatic differentiation, which is far more precise than numerical differentiation, allowing for meshless solvers [45, 69]. PINNs can integrate noisy data with PDEs, making them well-suited for inverse problems, even with non-linear relationships. They can also manage incomplete physics, aiding the development of self-modelling algorithms [47, 70]. Unlike purely data-driven neural networks, PINNs incorporate PDEs as regularisation terms, enabling them to handle sparse and incomplete data effectively.

However, PINNs come with certain limitations. Their training is specific and does not generalise like standard data-driven neural networks. Thus, each new PDE solution necessitates new training, making PINNs unsuitable for real-time or rapid predictions but better suited to determining precise solutions and to identifying innovative applications such as self-modelling. Additionally, as a relatively new methodology, PINNs lack a standard framework and may require parametric analyses for optimisation. In this work, we aim to lay the groundwork for efficient multi-diagnostic equilibrium reconstructions for tokamaks.

3.1. PINN architecture and training process

Figure 3(*a*) illustrates the neural network specifically designed for equilibrium reconstruction. The PINN takes the coordinates R and z, where plasma quantities need to be assessed, as inputs. The outputs are the potential vector A_ϕ, the toroidal magnetic field B_ϕ, the electron density N_e, and the electron temperature T_e. As mentioned, in this study we assume that the electron density N_e is equal to the ion density N_i and that the electron temperature T_e is equal to the ion temperature T_i. A physics layer is employed to calculate the poloidal magnetic field $B_{\mathrm{pol}} = (B_R, B_z)$ from the potential vector A_ϕ, and another layer evaluates the plasma pressure $p = 2N_eT_e$. Thus, in this

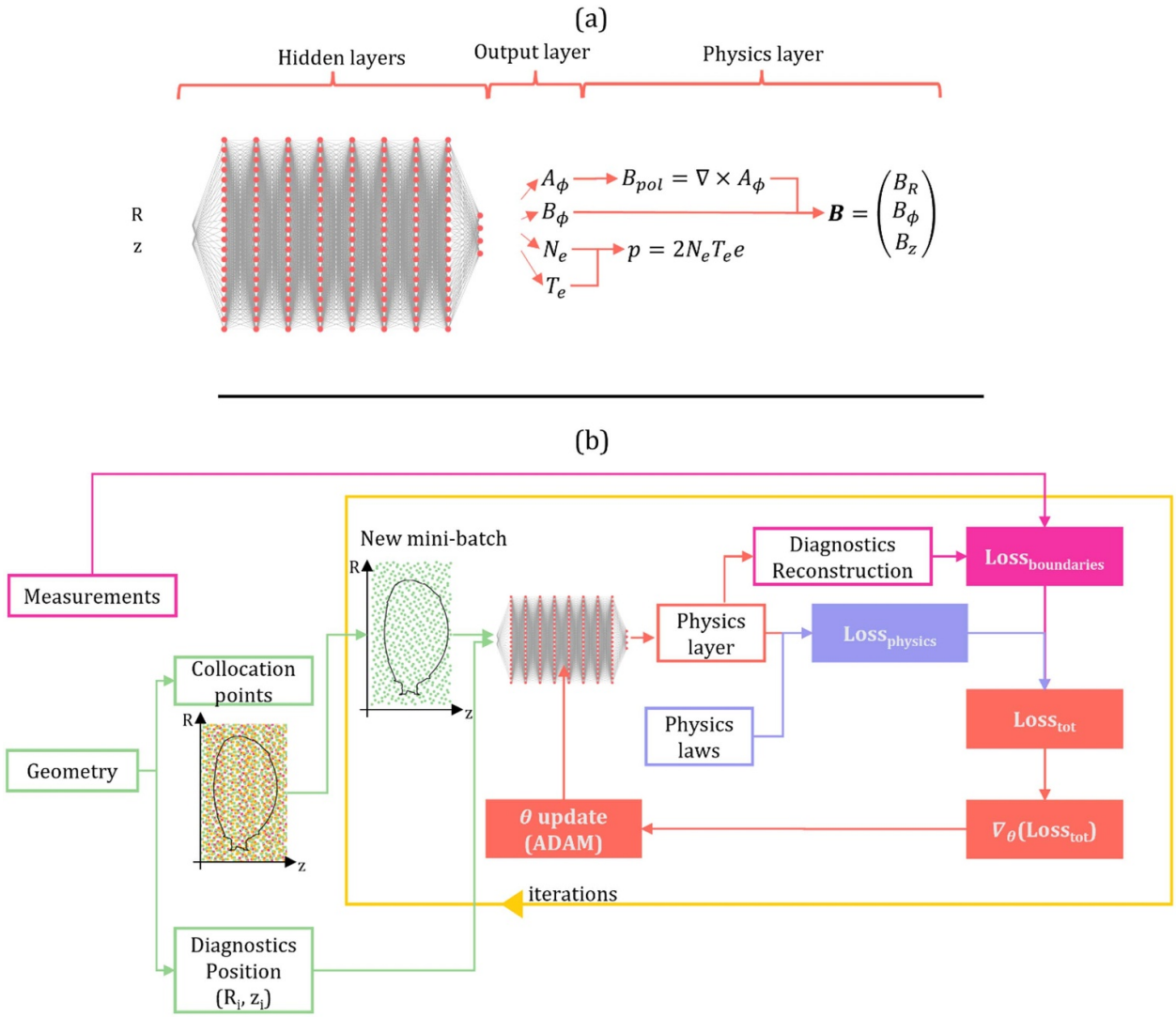

Figure 3. Schematic representation of the neural network used in this work for both TokaLab and JET cases (*a*) and schematic representation of the training algorithm (*b*). The bottom block diagram represents a single epoch: if the convergence criteria are not met at the end of 100 iterations, a new epoch is started.

specific case, the PINN is a function $F([R,z],\theta)$ that returns the plasma quantities given the coordinates. The neural network architecture implemented is a fully connected network with 8 hidden layers, each containing 20 neurons. The activation function is a hyperbolic tangent and biases are used. The non-linear transformation operated by each neuron can so be expressed as:

$$x_{\text{output}} = \tanh\left(w\, x_{\text{input}} + b\right). \tag{15}$$

Being x_{output} and x_{input} respectively the output and input of each neuron, w a multiplication factor called weight and b a constant called bias. The weight w together with the bias b constitute the network parameters θ. The overall number of parameters for the neural network used (see figure 3(*a*)) is 3084.

As usual the inputs to the network are normalised so that their absolute values are in the same range. To obtain physically meaningful quantities, the output layer (figure 3(*a*)) is then rescaled appropriately:

For TokaLab:

$$\begin{bmatrix} A_\phi \\ B_\phi \\ N_e \\ T_e \end{bmatrix} = \begin{bmatrix} 1 \\ 1 \\ 10^{20} \\ 10^{4} \end{bmatrix} \left\{ Y \begin{bmatrix} 1 \\ 1 \\ 0 \\ 0 \end{bmatrix} + Y \begin{bmatrix} 0 \\ 0 \\ \frac{e^{Y(3)}}{1+e^{0.9\,Y(3)}} \\ \frac{e^{Y(4)}}{1+e^{0.9\,Y(4)}} \end{bmatrix} \right\}.$$

For JET:

$$\begin{bmatrix} A_\phi \\ B_\phi \\ N_e \\ T_e \end{bmatrix} = \begin{bmatrix} 1 \\ 1 \\ 10^{19} \\ 10^{3} \end{bmatrix} \left\{ \boldsymbol{Y} \begin{bmatrix} 1 \\ 1 \\ 0 \\ 0 \end{bmatrix} + \boldsymbol{Y} \begin{bmatrix} 0 \\ 0 \\ \frac{e^{Y(3)}}{1+e^{0.9\,Y(3)}} \\ \frac{e^{Y(4)}}{1+e^{0.9\,Y(4)}} \end{bmatrix} \right\} \tag{16}$$

where Y is the output of the network, and the second term of the sum ensures the non-negativity of electron density and electron temperature (components 3 and 4 of the output). Multiplicative factors for electron density and temperature differences between TokaLab and JET are due to the different order of magnitudes of these two plasma quantities in the two scenarios (compare, for example, figures 4 and 8).

The parameters are fine-tuned using an iterative training process shown in figure 3(*b*). The training requires defining a loss term to minimise, which includes information from the boundaries and the physics model. To determine the boundary loss, diagnostic values must be calculated based on the reconstructed plasma quantities. These reconstructions are evaluated on the diagnostic points as described in section 3.2. The physics loss is calculated at the so-called collocation points, generated through a Sobol distribution [71, 72]. At each iteration, a subset (minibatch) of the collocation points is selected, and the neural network predicts the plasma quantities at these points. The resulting loss and the gradient of the loss with respect to the neural network parameters ($\nabla_\theta \mathrm{Loss_{tot}}$) are then calculated. The 'ADAM' algorithm is used to estimate the new neural network parameters, and a new iteration begins [73]. At the end of 100 iterations, if the convergence criteria are reached, the training ends, otherwise a new epoch consisting of 100 new iterations begins.

The minibatch size of the collocation points is 1000, and thus 100 000 collocation points are generated using the Sobol sequence.

A decaying learning rate is employed:

$$\text{Learning Rate} = \frac{\text{LearningRate}_0}{1 + \text{iteration} \cdot \text{LearningDecayRate}} \tag{17}$$

where $\text{LearningRate}_0 = 10^{-3}$ and $\text{LearningDecayRate} = 10^{-4}$.

At the end of each training epoch, a check is performed to determine if the stop condition is met. If the condition is satisfied, the training process halts, and the neural network is considered trained. Generally, the stop conditions are based on either a target value for the loss term (defining the desired accuracy), a threshold for the loss gradient (indicating no further improvement), or a maximum number of training epochs. In this work, the stop condition is the maximum number of epochs, set to 5000.

3.2. Loss function formulation and adaptive weighting scheme

As previously discussed, the minimisation of the loss function is central to the training of PINNs. In the context of PINNs, the loss is typically composed of two terms: the data (or boundary) loss and the physics loss:

$$\mathrm{Loss_{tot}} = \frac{\mathrm{Loss_{boundaries}} + \alpha\, \mathrm{Loss_{physics}}}{1+\alpha}. \tag{18}$$

Both $\mathrm{Loss_{boundaries}}$ and $\mathrm{Loss_{physics}}$ are expressed as the normalised mean squared error between the predicted value (the network output) and the desired target (either the measurements or the physical constraints):

$$\begin{aligned} \mathrm{Loss_{boundaries}} &= \sum \frac{w(y_p - y_b)^2}{W_{\mathrm{tot}}\sigma_b^2} \\ \mathrm{Loss_{physics}} &= \frac{1}{N}\sum \frac{(f(y_p) - f_{\mathrm{target}})^2}{C_f^2} \end{aligned} \tag{19}$$

where y_p is the predicted value, y_b is the measurement, σ_b is the measurement uncertainty, w is the diagnostic weight with respect to the total weight of the boundaries (W_{tot}), f_{target} is the physical equation describing the investigated phenomenon, and C_f is a suitable normalisation parameter.

The parameter α weights the relative importance of the two loss functions. Recent studies have demonstrated that balancing these two losses impacts the quality of the results significantly [74–76], especially when dealing with noisy data [76]. In a recent work, an adaptive weighting scheme optimised for inverse problems with noisy data was developed. This scheme is based on the consideration that while $\mathrm{Loss_{physics}}$ should converge to zero, $\mathrm{Loss_{boundaries}}$ has a different limit, which is a function of the measurement errors [77].

If the measurements used as boundary conditions were perfect (without noise or error), y_p would converge to y_b as the network trains, and $\mathrm{Loss_{boundaries}}$ would approach zero. However, real measurements are affected by random noise, and it can be shown that $(y_p - y_b)^2$ statistically converges to σ_b^2, making $\mathrm{Loss_{boundaries}}$ approach one. If $\mathrm{Loss_{boundaries}}$ reaches values much smaller than one, it is likely that the neural network is overfitting the noise. Therefore, an adaptive weighting scheme has been developed to ensure that $\mathrm{Loss_{boundaries}}$ converges to one and when this value is reached, the importance of the physics loss, i.e. α is increased.

This ensures that the neural network finds the optimal solution. At each epoch, $\mathrm{Loss_{boundaries}}$ is evaluated, and the weight parameter α is updated with the following equation:

$$\begin{aligned} \left(\frac{\Delta\alpha}{\alpha}\right)_{\mathrm{epoch}} &= 0.1 \tanh\left[-10\left(\frac{\mathrm{Loss_{boundaries}\,(epoch)}}{\mathrm{Loss_{target}}} - 1\right)\right] \\ \alpha_{\mathrm{epoch}} &= \alpha_{\mathrm{epoch}-1}\left(1 + \left(\frac{\Delta\alpha}{\alpha}\right)_{\mathrm{epoch}}\right) \\ \alpha_{\mathrm{epoch}} &= \max\left(\alpha_{\mathrm{epoch}}, \alpha_{\mathrm{min}}\right) \end{aligned} \tag{20}$$

where the last equation ensures that α_{epoch} does not fall below a minimum value to avoid training saturation at a local minimum representing a non-physical solution. Empirically, α_{min} has been set to 0.01. From a practical standpoint, due to statistical considerations, it is advisable to increase the ideal $\mathrm{Loss_{target}}$ by a numerical factor. In ideal cases (no noise), the final target would be zero, but this would imply that α would never increase. For noisy data, the target of one is true only for an infinite number of measurements. A value of 1.5 has been found to be a good choice for achieving accurate reconstructions. A discussion on the impact of $\mathrm{Loss_{target}}$ selection has been detailed in previous works [77]. In this study, $\mathrm{Loss_{target}}$ is set to 1.5.

Details about the calculation of the loss boundaries including each diagnostic modelling are described in appendix A

while information about the uncertainties and configurations for both TokaLab and JET are reported in table 1.

With regard to the physics losses, a soft-constrained approach is used by considering the MHD equilibrium through the set of equation (2) instead of the Grad–Shafranov formulation (3). Indeed, assuming the MHD equilibrium through (3) means imposing the hard constraint that the kinetic profiles are a function of the magnetic flux ψ. While this could be useful to accelerate the convergence of the PINN algorithm, we would like to develop a more-flexible tool to test a less-constrained algorithm, opening the prospect of including additional effects, such as plasma rotation, and of addressing time dependent MHD, multi-fluid MHD and core-edge integration problems.

The loss physics therefore is made of five terms which consider the error on the plasma MHD equations (pressure balance), the vacuum MHD equations (pressure and density current equal to zero), boundaries from physics (i.e. the fact that the plasma quantities are zero on the wall), and two regularisation terms, which favours smooth solutions for the density and temperature profiles in the parallel and orthogonal directions, with a smaller constraint along the orthogonal direction. These five terms have been normalised to ensure that they are balanced. Details about their formulations are provided in appendix A.

4. Results

This section is mainly divided in two parts. The first part analyses the PINN performances for the synthetic scenarios using TokaLab. The synthetic scenarios allow for direct performance evaluations since they are numerical solutions of the Grad–Shafranov equation. They have been used to calculate the synthetic measurements and therefore they are the target the reconstruction algorithm should converge to. They are also referred to as ground truth.

More specifically, this first part of the section reports the following analyses:

1. The first analysis illustrates the importance of using multi-diagnostic constraints to converge on accurate results, showing also the capability of the multi-diagnostic approach to filter out outliers or faulty diagnostics.
2. Performance evaluation of the PINN algorithms for four different scenarios relevant for tokamaks, i.e. the SN, the Double Null (DN), the Negative Triangularity (NT), and Inverted q-profile (IQ). The scope of this first analysis is to prove the capability of PINNs to reconstruct different types of equilibria.
3. The last synthetic analysis briefly illustrates the importance of high-fidelity modelling of plasma diagnostics, by referring to the IP diagnostics, which requires both the inclusion of the hot plasma assumption (relativistic effects) and modelling of the non-linear interactions between Faraday rotation and Cotton–Mouton phase shift.

Then, a second section focuses on experimental analyses performed on JET pulses. In this case, the ground truth is unknown and therefore a different approach is used to corroborate accuracy and reliability. This section is then divided into the following parts:

1. Diagnostic ablation tests: one diagnostic is removed from the PINN constraints and used as independent diagnostic for the test.
2. Comparison with advanced equilibrium reconstruction codes typically used at JET.
3. Application to advanced baseline and hybrid pulse scenarios.

4.1. Synthetic cases

As mentioned, the first synthetic case modelled with TokaLab consist of a virtual tokamak with a major geometrical radius $R_0 = 6$ m and the minor radius $a = 2$ m in a SN configuration, with a plasma current of 12 MA, a toroidal field of 5 T. In the numerical simulation, a pressure of 100 Pa at the LCFS is imposed. Gaussian noise is added to each diagnostic with the standard deviations reported in table 1. Figure 4 shows the target quantities computed with TokaLab (top row), the reconstructed fields using the PINN (middle row), and the differences between them (bottom row). This case has been calculated using all the set of diagnostics (Magnetics, TS, IP, and MSE). From a qualitative point of view, one can see that the reconstructed quantities are very close to the true values, as confirmed by the small values of the errors.

Quantitative results shown in table 2, where the reconstruction errors (in terms of RMSE) and the goodness of fit (R^2) for the main plasma quantities are reported as a function of the diagnostic used as constraints. By increasing the number of diagnostics from 'Magnetics + Thomson scattering' to 'Magnetics + Thomson scattering + Interferometer-Polarimeter' and 'Magnetics + Thomson scattering + Interferometer-Polarimeter + Motional Stark Effects' leads to clear improvements to all reconstructed quantities. Indeed, increasing the number of diagnostics increases the quantity of information and, so, the model capability of reconstructing the equilibrium.

Figure 5 reports the errors (in relative terms, calculated as $1 - R^2$) on the kinetic profiles as a function of the flux coordinate $N_e(\psi)$ and $T_e(\psi)$. The figure shows that also the reconstruction of these quantities improves by adding more diagnostics, as expected.

The reconstructed fields are compared with the target in figure 4 where the RMSE of the residuals are also shown. The robustness of the algorithm has been tested by repeating 3 times the reconstructions with all the diagnostics. Table 3 reports the uncertainty of RMSE and R^2 for this case, showing very good stability of the solutions.

Using a multi-diagnostic approach together with the implemented adaptive weighting scheme allows to easily filter out outliers, offsets and diagnostic faults. As example, let us suppose that a measurement is severely anomalous due to a faulty

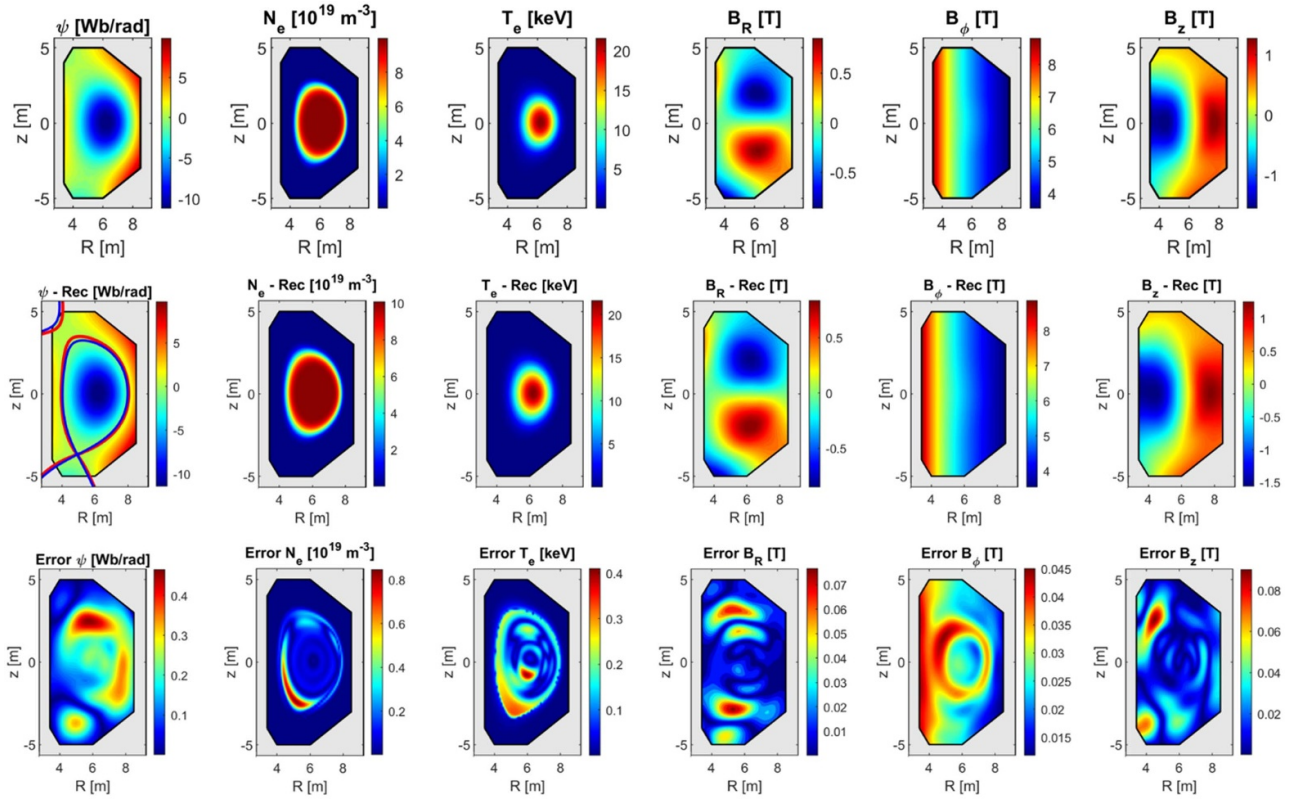

Figure 4. Top row: target fields. Centre row: reconstructed fields. Bottom row: RMSE for the last case of table 2.

Table 2. Reconstruction performance improvement by increasing the number of diagnostics. Unit of measurements are (Wb rad^{-1}) for ψ, (m^{-3}) for N_e, (eV) for T_e and (T) for all the B components.

		ψ	N_e	T_e	B_R	B_ϕ	B_z
Magnetics + Thomson Scattering	RMSE	7.58×10^{-1}	3.68×10^{18}	5.50×10^{2}	9.50×10^{-2}	4.21×10^{-2}	1.12×10^{-1}
	R^2	92.20 %	98.87 %	98.30 %	86.19 %	99.98 %	95.23 %
Magnetics + Thomson Scattering + Interferometer-Polarimeter	RMSE	1.24×10^{-1}	2.11×10^{18}	2.68×10^{2}	2.22×10^{-2}	2.74×10^{-2}	3.69×10^{-2}
	R^2	99.86 %	99.61 %	99.56 %	99.51 %	99.99 %	99.59 %
Magnetics + Thomson Scattering + Interferometer-Polarimeter + Motional Stark Effect	RMSE	1.07×10^{-1}	7.92×10^{17}	1.09×10^{2}	1.01×10^{-2}	2.16×10^{-2}	1.24×10^{-2}
	R^2	99.90 %	99.95 %	99.92 %	99.90 %	99.99 %	99.96 %

SL, the one indicated in figure 1. The outlier has been modelled with the following equation:

$$\text{Outlier}_{\text{SL}} = \text{Modelled}_{\text{SL}} + 4\,\sigma_{\text{SL}}. \tag{21}$$

That is equivalent to a systematic error ∼50% (offset equal to 0.200 Wb rad^{-1} with respect to the ideal value of −0.396 Wb rad^{-1}). All the other measurements are affected by the previously mentioned basic level of noise. The PINN reconstruction, shown in figure 6, is again very close to the target, as also quantified in table 4, with an error comparable with the statistics previously described. This particular PINN robustness against offsets and outliers is due to the combination of the multi-diagnostic approach and physics constraints, which implies that there are not alternative solutions that are in line with both the physics and the other diagnostics.

Another important study has consisted of assessing the flexibility of the PINNs in reconstructing different plasma scenarios. To verify this, as previously anticipated, the PINN has been applied to other typical plasma scenarios: a DN, a NT and a SN with IQ. The descriptions of how these scenarios have been generated and all the target, reconstructed, and error fields can be found in appendix C. In this subsection only the main statistics (table 5) and comparisons with the magnetic flux (figure 7) are reported. The results clearly show that the PINN performances are stable also for other plasma scenarios, verifying the generality of the methodology.

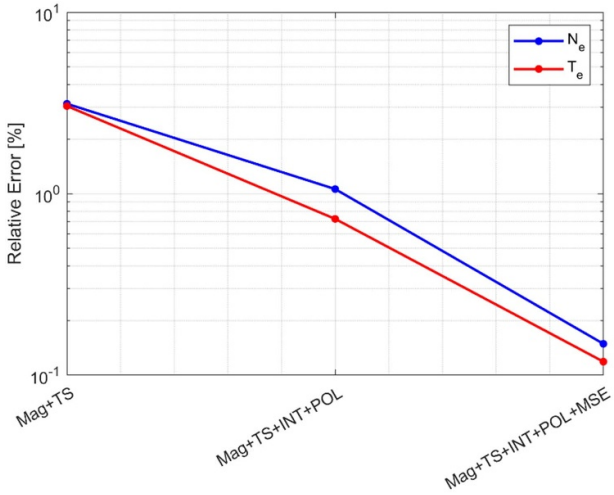

Figure 5. Relative error on $N_e(\psi)$ and $T_e(\psi)$ increasing the number of diagnostics.

Table 3. Algorithm robustness in terms of standard deviation of RMSE and R^2 for the three repetitions of the reconstruction.

	ψ	N_e	T_e	B_R	B_ϕ	B_z
σ_{RMSE}	3.49×10^{-3}	2.22×10^{17}	1.28×10^{2}	1.12×10^{-3}	9.35×10^{-3}	4.5×10^{-3}
σ_{R^2}	0.01%	0.05%	0.31%	0.03%	∼0%&	0.07%

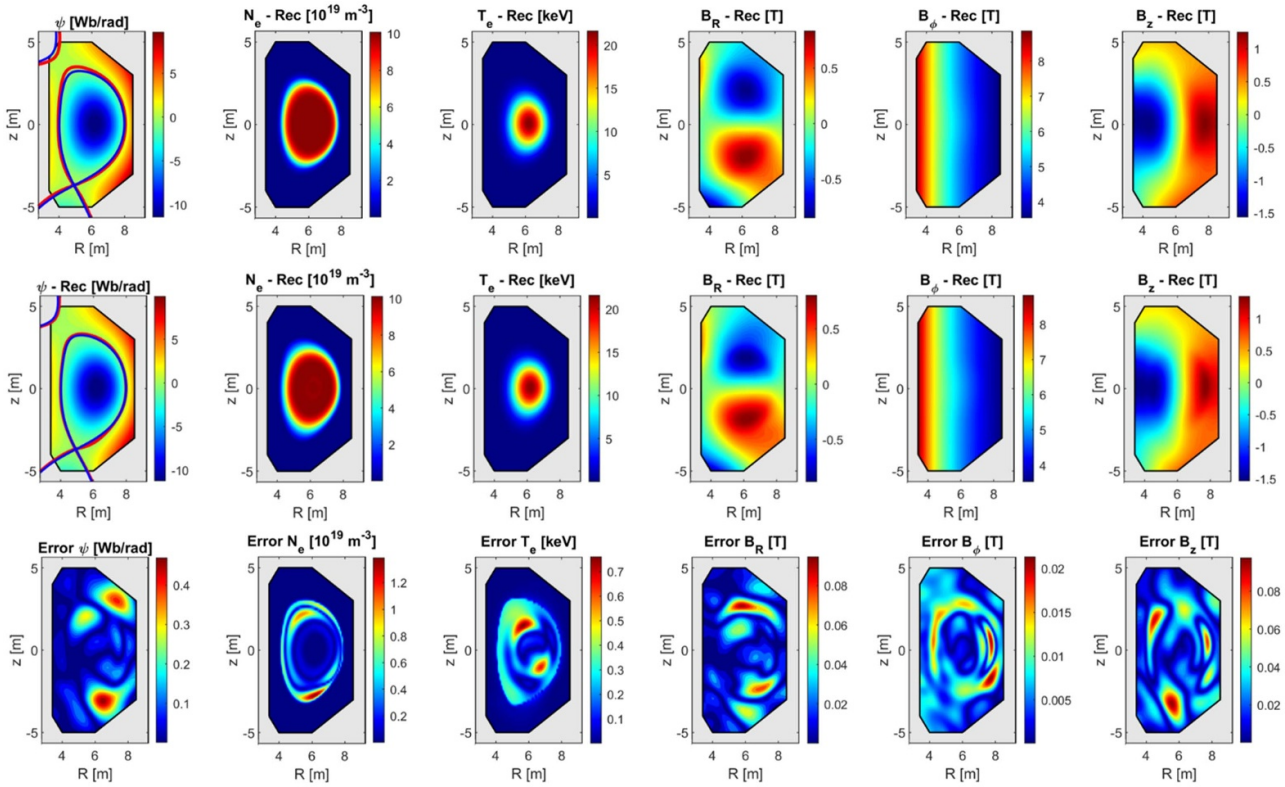

Figure 6. Case with a saddle loop affected by a systematic error, becoming an outlier. Top row: target fields. Centre row: reconstructed fields. Bottom row: RMSE.

The last important consideration, confirming and extending what already discussed in [55], is the need for high-fidelity modelling of the diagnostics. This is important for diagnostics such as interferometers and polarimeters, whose measurements are not direct local quantities, but are line-integrated complex functions that can be affected by non-linearities (see type-I vs Stokes polarisation modelling) [55] and hot plasma (e.g. relativistic) effects [78]. (Full Stokes hot

Table 4. Reconstruction performance comparison in terms of RMSE and R^2 without the outlier and with the outlier. Unit of measurements are (Wb rad^{-1}) for ψ, (m^{-3}) for N_e, (eV) for T_e and (T) for all the magnetic field components.

		ψ	N_e	T_e	B_R	B_ϕ	B_z
Without outlier	RMSE	1.07×10^{-1}	7.92×10^{17}	1.09×10^{2}	1.01×10^{-2}	2.16×10^{-2}	1.24×10^{-2}
	R^2	99.90%	99.95%	99.92%	99.90%	99.99%	99.95%
With outlier	RMSE	1.08×10^{-1}	2.10×10^{18}	1.46×10^{2}	2.09×10^{-2}	5.57×10^{-3}	2.37×10^{-2}
	R^2	99.90%	99.62%	99.86%	99.56%	100.00%	99.83%

Table 5. Goodness of fit between true and reconstructed fields for the four scenarios.

	SN	TN	DN	IQ
ψ	99.78%	99.87%	99.59%	99.92%
N_e	99.88%	99.89%	99.71%	99.94%
T_e	99.95%	99.93%	99.79%	99.61%
B_R	99.62%	99.85%	99.54%	99.58%
B_ϕ	99.99%	99.98%	99.96%	99.96%
B_z	99.87%	99.93%	99.76%	99.90%

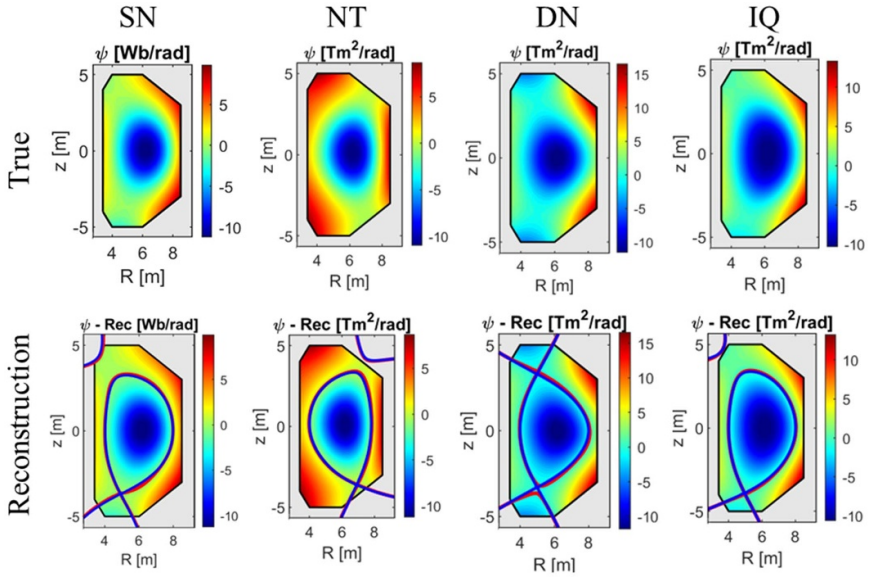

Figure 7. True (top) vs reconstructed (bottom) magnetic flux for the single null (SN), negative triangularity (NT), double null (DN) and inverted q-profile (IQ) scenarios.

Table 6. Goodness of fit for the TokaLab reference scenario in case of different fidelity levels of the interferometer-polarimeter diagnostic models.

	ψ	N_e	T_e	B_r	B_ϕ	B_z
Type-I—cold plasma	94.27%	99.88%	99.98%	94.35%	98.57%	92.88%
Full Stokes—cold plasma	99.06%	97.18%	99.16%	94.87%	99.41%	97.46%
Full Stokes—hot plasma	99.90%	99.98%	99.92%	99.90%	∼100%	99.96%

plasma) includes also the hot plasma effects on both interferometer and polarimeter. In this last simulation, very accurate results are obtained, showing the importance of modelling correctly the diagnostics to achieve accurate reconstructions.

Table 6 shows the goodness of fit for the SN TokaLab scenario in three cases. In the first case (Type-I Cold Plasma), both the polarimeter and the interferometer are modelled assuming a cold plasma and the polarimeter implements the type-I approximation. In this case, the errors are quite high considering that the measurements in this case are perfect (no random noise has been added). The second example (Full Stokes cold plasma) models the non-linear interaction between Faraday rotation and Cotton–Mouton phase shift but again in the cold plasma approximation, while the last case (Full

Table 7. Algorithm robustness in terms of mean and standard deviation of RMSE and R^2 for pulse 89724. Unit of measurements are (Wb rad^{-1}) for, (Pa) for p, (T) for all the B components, (A) for all the J components.

	ψ	p	B_R	B_ϕ	B_z	J_R	J_ϕ	J_z
$\overline{\text{RMSE}}$	2.19×10^{-2}	4.43×10^{3}	9.55×10^{-3}	8.49×10^{-2}	7.37×10^{-3}	2.45×10^{3}	3.70×10^{4}	4.20×10^{3}
σ_{RMSE}	3.69×10^{-3}	9.87×10	1.34×10^{-3}	9.05×10^{-4}	6.84×10^{-4}	6.21×10^{2}	1.71×10^{3}	1.03×10^{3}
$\overline{R^2}$	99.87%	89.23%	99.68%	99.73%	99.93%	99.26%	99.31%	98.89%
σ_{R^2}	0.04%	0.48%	0.09%	0.01%	0.01%	0.33%	0.06%	0.47%

Stokes hot plasma) includes also the hot plasma effects on both interferometer and polarimeter. In this last simulation, very accurate results are obtained, showing the importance of modelling correctly the diagnostics to achieve accurate reconstructions.

Complementary quantities for the performances of the equilibrium reconstruction in the synthetic case can be found in appendix D. In the same section, a discussion on the benefits of automatic differentiation is also provided.

4.2. Application of the PINN technology to JET data and validation of the results

In this section, the results obtained by applying the PINN technology to JET experimental data are shown. In this case, the ground truth is unknown and therefore some indirect confirmations of the method quality are needed:

1. Firstly, a comparison analysis of the reconstruction with EFIT, the standard equilibrium reconstruction code of JET, for pulse #89724. This comparison is performed to ensure that the PINN does not return absurd results, while small differences cannot be directly attributed to EFIT or to the PINN method error, since the ground truth is not known. Even in this case, robustness and sensitivity to outliers are analysed.
2. For the same pulse, a second form of validation consists of analysing the compliance with the physical equations. In detail, this is achieved by evaluating how the solutions fit the Grad–Shafranov equation. The detected errors are compared also with the EFIT errors.
3. A diagnostic ablation analysis has also been performed. This test consists of removing one diagnostic from the PINN constraints, reconstruct the equilibrium, and compare the predictions of ablated diagnostics with the actual measurements.
4. At the end, a comparison between the EFTF, EFTP, and PINN reconstructions is discussed for pulse #96996. An evaluation of diagnostics reconstruction errors is provided. The benefits of increasing number of diagnostics on boundary conditions reconstruction are in line with finding presented in [79]. The error committed in fitting the Grad–Shafranov equation are comparable with the ones from EFTF.

Table 7 reports the RMSE and R^2 between PINN and EFIT, showing good agreement for all MHD fields, with a larger error observed for the pressure. This was expected since EFIT is not constrained with a pressure diagnostic, making the core ill-posed. The standard deviation of both RMSE and R^2, done by replicating the PINN reconstruction three times, show high robustness of the method. The reconstructed fields using EFIT and PINN on pulse 89724 are shown in figure 8, with also the illustration of the q profile as a function of the poloidal flux coordinate. The PINN reconstruction, figure 8(b), is plotted on a more extended grid with respect to the EFIT's one. This is to show the interesting reconstruction of magnetic fields inside the divertor coils.

Table 8 reports the RMSE and the R^2 evaluated by comparing the case with and without the outlier, added following the same procedure for the TokaLab analysis. The results validate the low sensitivity of the PINN method to outliers.

Figure 9 shows the probability density distribution (left) and the cumulative density function (right) of the errors in the fit of the Grad–Shafranov equation committed by EFIT (in blue) and PINN (in red) for JET pulse 89724. The errors are evaluated on the same grid, the one used by EFIT. The results show that both methods are characterised by almost the same distributions, with PINN showing a smaller tail. The RMSE values obtained for the two cases are 2.41 (Wb(m^2 rad)$^{-1}$) for EFIT and 2.35 (Wb(m^2 rad)$^{-1}$) for the PINN. This confirms that both the PINN and EFIT converge on the same physical solution.

The ablation test is conducted by removing a different diagnostic each time, training the algorithm and evaluating its performance in reconstructing the measurements of the ablated diagnostic and the plasma quantities of interest. The TS has been treated slightly differently by ablating in turn the electron density measurements (case indicated in the table as TS-N_e) and the electron temperature measurements (TS-T_e). Table 9 shows the ablation results by evaluating the RMSE (top) and the Pearson coefficients (middle) between the reconstructed and ablated diagnostics and by comparing the reconstructed fields with and without ablation (bottom).

The largest errors in diagnostic reconstructions are obtained, as expected, for the diagnostic that is ablated. Regarding MHD-related diagnostics (PU, FL, SL), the ablation has not important effects on the reconstruction. Indeed, PU and SL show small RMSE error, high Pearson coefficient and high R^2. The FL case has high RMSE and low R^2 on the FL and magnetic flux reconstruction. However, this error is given by an offset that it is physically expected. Indeed, if the FL are not used, there are infinite solutions ψ_i described by $\psi_i = \psi_{\text{true}} + c$, where c is a constant. This is demonstrated by the fact that the comparison on normalised magnetic flux ψ_n is quite good, since this loses the offset

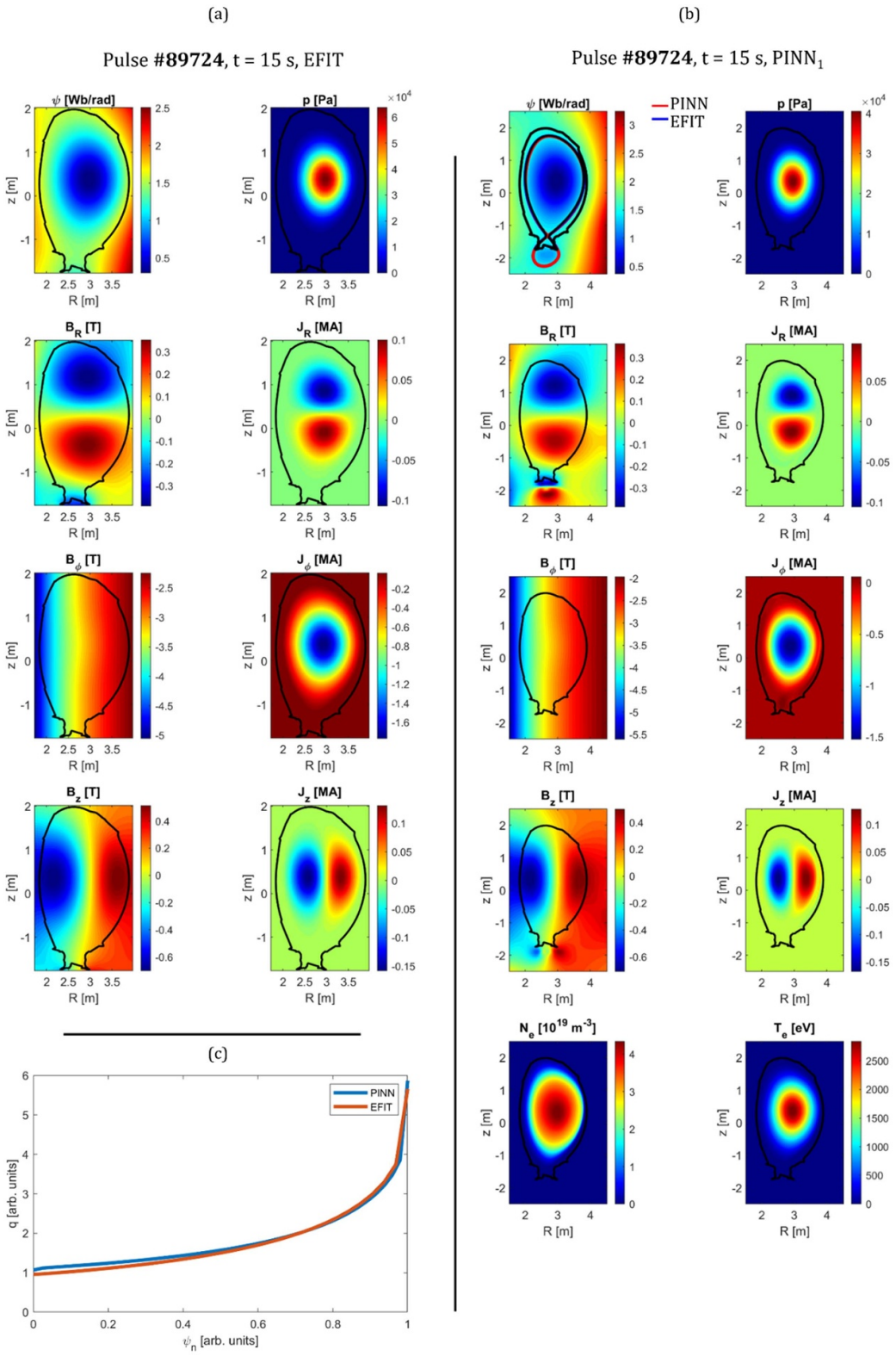

Figure 8. Pulse reconstruction at $t = 15$ s with EFIT (a), PINN (b) and $q(\psi)$ profile (c).

information. Moreover, all other fields have high R^2 and the Pearson coefficient between measurements and reconstructed FL is high. Coherent results have been also obtained for the kinetic fields. In the case of TS-N_e, LID and Far, the ablation tests show good stability, with small degradation of the performance in the case of TS-N_e. This is interpreted as a consequence of the fact that TS-N_e is the only diagnostic with high information content (local measurements from edge to core), while the IP is characterised by a small number of lines of sight (8 total lines, 6 used for the interferometer and 4 for the

Table 8. PINN reconstruction performances for the case with one outlier. The target, in this case, is the PINN reconstruction without outliers. Unit of measurements are (Wb rad^{-1}) for ψ, (Pa) for p, (T) for all the B components and (A) for all the J components.

	ψ	p	B_R	B_ϕ	B_z	J_R	J_ϕ	J_z
RMSE	3.68×10^{-3}	3.28×10^{2}	3.01×10^{-3}	5.18×10^{-3}	2.20×10^{-3}	1.07×10^{3}	1.76×10^{4}	1.29×10^{3}
R^2	100.00%	99.88%	99.97%	100.00%	99.99%	99.88%	99.84%	99.92%

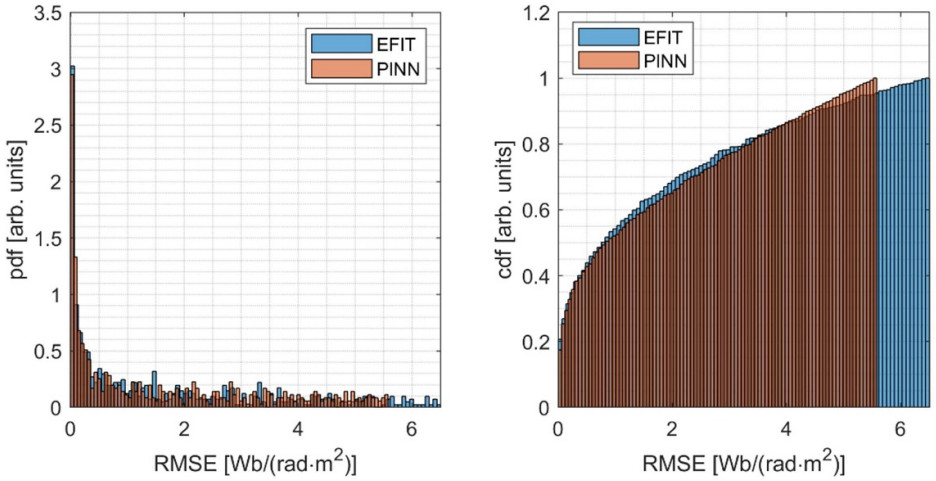

Figure 9. Pulse 89724. Absolute error distribution in the fit of the Grad–Shafranov equation for both EFIT reconstruction (blue) and PINN reconstruction (orange).

polarimeter) and by a less informative type of measurement (line-integrated). A worse result is obtained also when ablating the TS-T_e, since this is the only diagnostic used to constrain the electron temperature. However, the performances are still quite respectable (R^2 on T_e field $\sim$87%) thanks to the multi-diagnostics approach. Indeed, the pressure, density and temperature are interrelated and therefore the temperature is reconstructed by using the information from the density profile and from the pressure, evaluated combining the constraints from the data and the physics.

Figure 10 shows the measured against the reconstructed TS data for both electron density and temperature in two distinct cases, named PINN_0 and PINN_1. In the case of PINN_0, the standard deviations of the TS variables have been evaluated using the methodology described in section 2. However, this standard deviation is quite high, and the PINN reconstructs a less steep density profile. By decreasing the standard deviation on the pedestal by a factor 5, the results are the ones shown by PINN_1, where the reconstructed density profile follows the measured one much more closely.

In the case of figure 10, the PINN reconstruction results are the ones previously called 'PINN_1', and so the ones with the imposition of narrower uncertainties on the TS. The magnitude of the reconstructed density and temperature are in line with the results reported in the literature [57], even if the magnitude of the PINN-reconstructed pressure is not completely coherent with EFIT. On the other hand, the magnetic field reconstructions are in agreement with the ones from EFIT.

This result clearly suggests that the definition of the standard deviation plays a key role, especially in cases where there is no other good information for the same plasma quantity. This is the case of the electron density, which in H-mode shows a steep gradient in the pedestal region. This effect is not modelled in the PINN, since there are no physical equations (e.g. no transport model) able of reproducing this strong gradient. At the same time, the other relevant diagnostic, the interferometer, provides line-integrated information, in which the detailed local information is lost. In brief, these results suggest that:

1. If there are no other sources of information, it might be advantageous to increase the constraints on specific diagnostics, by decreasing their uncertainty.
2. If diagnostics are not reliable, it is fundamental to implement a multi-diagnostic approach or insert physical models able to inform the PINN about poorly measured quantities.

Comparisons with more advanced EFIT algorithms have been also performed. The first one, named EFTP, implements a pressure constraint using the high-resolution TS measurements, while the second, named EFTF, implements also the constraint of the Faraday rotation, even if it is modelled with the type-I cold-plasma approximation. A comparison with these codes has been conducted for pulse #96996.

Figure 11 shows the comparison between the reconstructed magnetic flux fields both for EFTF and for PINN. The relative error is mainly located in the core region. In this case, average errors fitting the Grad–Shafranov equation are 2.38 (Wb(m^2 rad)$^{-1}$) for EFTF and 2.31 (Wb(m^2 rad)$^{-1}$) for the PINN, in line with the errors evaluated for pulse #89724.

Table 9. Pulse 89724. RMSE and Pearson coefficients of diagnostic reconstruction in the ablation test and the reconstructed fields performances through R^2. Units of measurement are (T) for PU, (Wb rad^{-1}) for FL and SL, (m$^{-3)}$ for TS (N_e) and (eV) for TS (T_e), (m^{-2}) for LID and (rad) for Far.

	Diagnostics—RMSE						
	PU	FL	SL	TS-N_e	TS-T_e	LID	Far
No ablation	$\mathbf{6.74 \times 10^{-3}}$	$\mathbf{7.65 \times 10^{-3}}$	$\mathbf{1.01 \times 10^{-2}}$	$\mathbf{2.09 \times 10^{18}}$	$\mathbf{1.13 \times 10^{2}}$	$\mathbf{5.15 \times 10^{17}}$	$\mathbf{1.52 \times 10^{-2}}$
PU	$\mathbf{3.36 \times 10^{-2}}$	7.33×10^{-3}	1.19×10^{-2}	2.25×10^{18}	1.20×10^{2}	5.65×10^{17}	1.30×10^{-2}
FL	8.39×10^{-3}	**2.42**	9.23×10^{-3}	2.16×10^{18}	1.23×10^{2}	5.91×10^{17}	1.24×10^{-2}
SL	6.91×10^{-3}	3.88×10^{-3}	$\mathbf{3.11 \times 10^{-2}}$	2.34×10^{18}	1.21×10^{2}	5.22×10^{17}	1.25×10^{-2}
TS-N_e	6.52×10^{-3}	6.78×10^{-3}	1.29×10^{-2}	$\mathbf{3.66 \times 10^{18}}$	1.39×10^{2}	6.30×10^{17}	1.56×10^{-2}
TS-T_e	8.86×10^{-3}	7.62×10^{-3}	1.36×10^{-2}	1.93×10^{18}	$\mathbf{8.41 \times 10^{2}}$	6.12×10^{17}	2.39×10^{-2}
LID	8.28×10^{-3}	7.49×10^{-3}	1.29×10^{-2}	1.66×10^{18}	1.16×10^{2}	$\mathbf{1.99 \times 10^{18}}$	1.29×10^{-2}
Far	1.04×10^{-2}	7.03×10^{-3}	1.41×10^{-2}	1.58×10^{18}	1.17×10^{2}	3.39×10^{17}	$\mathbf{1.84 \times 10^{-2}}$
	Diagnostics—Pearson coefficient						
	PU	FL	SL	TS-N_e	TS-T_e	LID	Far
No ablation	99.97%	99.94%	99.95%	99.07%	99.27%	99.99%	99.81%
PU	99.53%	99.94%	99.93%	98.92%	99.19%	99.99%	99.89%
FL	99.96%	98.88%	99.96%	99.01%	99.16%	99.98%	99.88%
SL	99.96%	99.98%	99.56%	98.77%	99.15%	99.99%	99.87%
TS-N_e	99.97%	99.93%	99.92%	97.03%	98.89%	99.98%	99.84%
TS-T_e	99.95%	99.93%	99.91%	99.19%	98.89%	100.00%	99.16%
LID	99.95%	99.94%	99.92%	99.36%	99.25%	99.98%	99.82%
Far	99.93%	99.93%	99.90%	99.45%	99.22%	100.00%	99.54%
	Ablated reconstructed fields R^2 respect with not ablated reconstruction									
	ψ	N_e	T_e	B_R	B_ϕ	B_z	J_R	J_ϕ	J_z	ψ_n
PU	99.88%	99.65%	99.76%	99.76%	99.99%	99.78%	98.99%	99.22%	99.03%	99.97%
FL	−418%	99.45%	99.80%	99.88%	99.91%	99.97%	99.71%	99.74%	99.63%	99.94%
SL	99.99%	99.90%	99.82%	99.95%	100.00%	99.98%	99.78%	99.79%	99.68%	99.99%
TS-N_e	99.99%	99.64%	99.81%	99.95%	100.00%	99.99%	99.71%	99.88%	99.77%	99.99%
TS-T_e	99.98%	99.42%	87.15%	99.92%	99.46%	99.91%	98.88%	99.58%	98.69%	99.97%
LID	99.97%	98.40%	99.69%	99.87%	100.00%	99.96%	99.33%	99.63%	99.25%	99.98%
Far	99.99%	99.17%	99.55%	99.87%	99.99%	99.95%	99.04%	99.67%	99.23%	99.98%

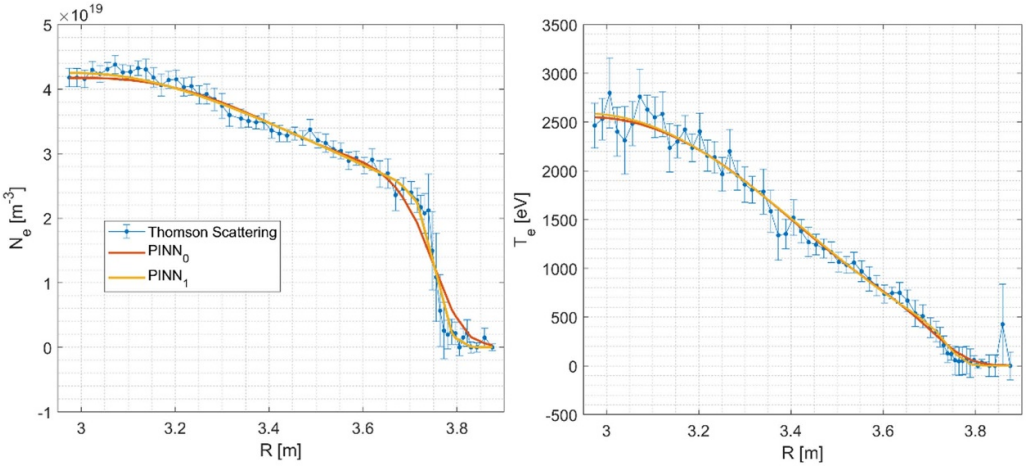

Figure 10. Pulse 89724. Reconstructed vs measured (HRTS) density and temperature profiles.

As it happens for the PINN, also in the case of EFIT increasing the number of diagnostics results in an improvement of the reconstruction quality [79].

Table 10 shows the RMSE between reconstructed diagnostics (given the equilibrium) and the measurements for EFTP, EFTF, and multi-diagnostic PINN. The error between

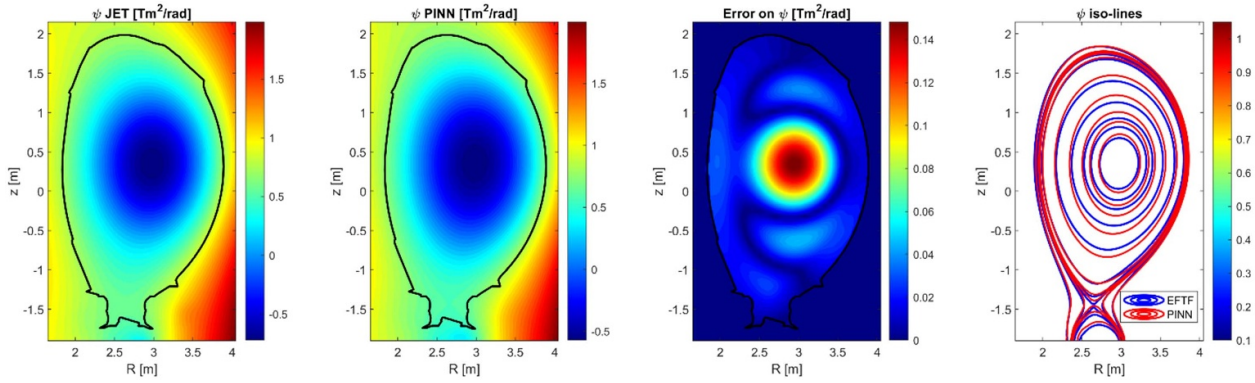

Figure 11. Pulse 96996. Reconstruction of magnetic flux ψ with EFTF (first on the left) and PINN (second). The respective RMSE map is shown on the third plot and the magnetic flux lines on the right.

Table 10. Comparison between EFTP, EFTF and multi-diagnostic PINN equilibrium reconstructions for pulse 96996.

	PU [T]	FL [T]	SL [T]	p-TS [Pa]	LID [m^{-2}]	Far [rad]
EFTP	1.36×10^{-2}	2.03×10^{-2}	1.31×10^{-2}	1.30×10^{4}	—	—
EFTF	1.38×10^{-2}	2.33×10^{-2}	1.35×10^{-2}	5.90×10^{3}	9.04×10^{19}	3.68×10^{-1}
PINN	7.21×10^{-3}	5.24×10^{-3}	1.10×10^{-3}	5.28×10^{3}	5.87×10^{19}	3.00×10^{-1}

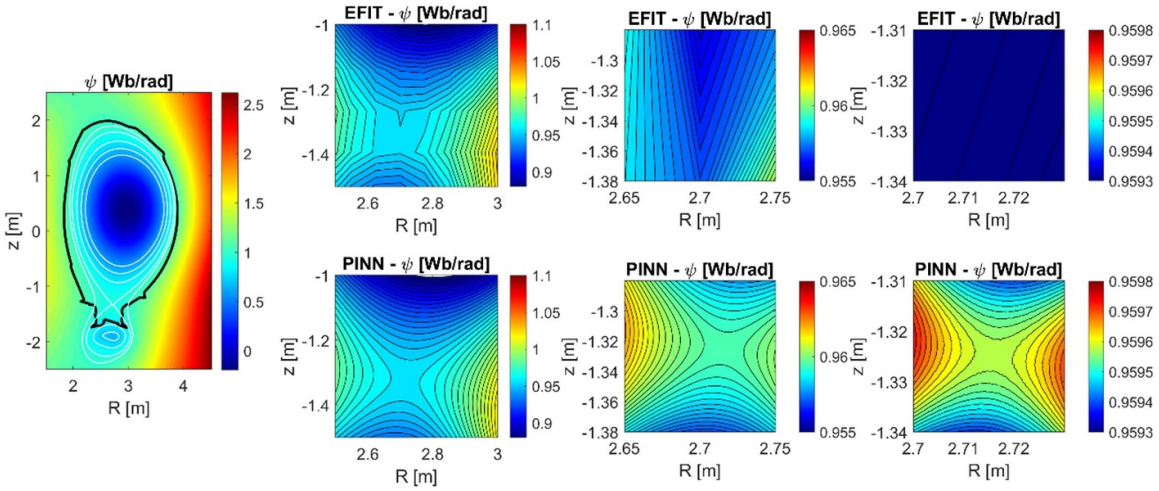

Figure 12. Pulse 89724. Example of super-resolution. Zoom in of the X-point in an area of 9 cm^2.

the reconstructed diagnostics and the measurements are small and in line with their uncertainty, and this was expected since they are used to constrain the models. As mentioned before, in this case it is not possible to evaluate the accuracy of each model since the ground truth is unknown. However, the good accordance with the measurements together with small errors in the fit of the Grad–Shafranov equation suggests that the PINN provides good solutions.

Before moving to the application of PINN to high-performance pulses, it is worth introducing another PINN feature known as super-resolution [80, 81]. Indeed, contrary to standard computational methods, which evaluate the quantities in a discretised domain, PINNs predict holistically entire functions. These functions are obtained by training on a huge amount of collocation points, which are sub-sampled at each iteration. This implies that the PINNs are trained on a highly resolved space, and that therefore they can provide information at small scales without applying any interpolation. This aspect is shown in figure 12. The top row shows the fields around the X-point by zooming at increasingly smaller scales, showing that the X-point is lost just at the second image, since the zoom is comparable with the EFIT grid. On the contrary, the bottom row shows the output of the PINN, and it is evident that the X-point shape is conserved at smaller scales. This feature can be relevant in various applications where small-scale phenomena occur, like in turbulence, or in the reconstruction of quantities that show different scales across different directions, as occurs in the scrape-off layer.

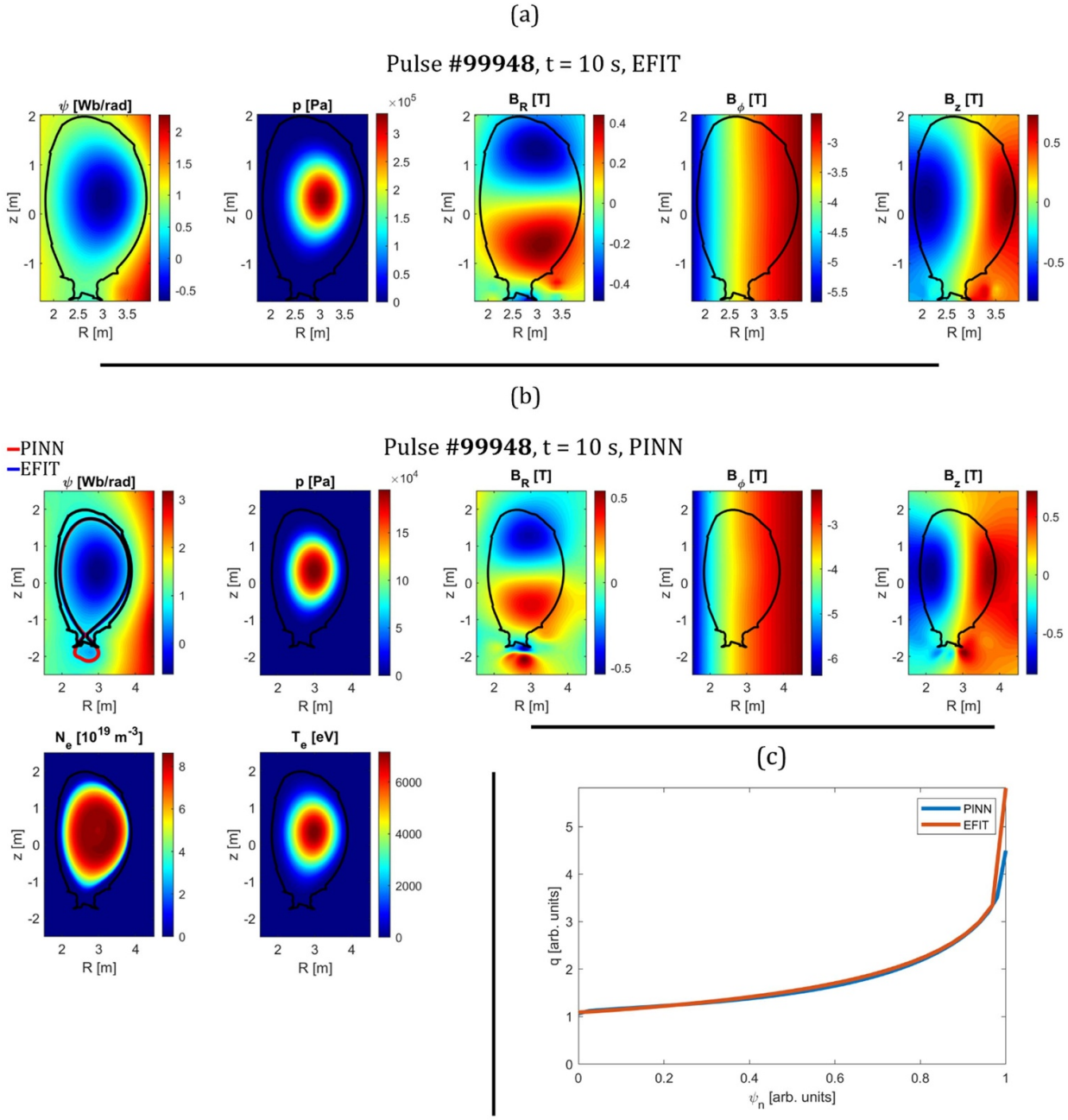

Figure 13. Pulse #99948 ($t = 10$ s). EFIT reconstruction (a) vs PINN reconstruction (b) and q profile (c).

4.3. Application to high-performance pulses

This section illustrates the application of the PINN equilibrium reconstruction algorithm to two high-performance pulses at the JET. The first pulse, numbered 99948, is a D–T baseline scenario with a toroidal field of 3.3 T, a plasma current of 3.5 MA, additional heating power of approximately 29 MW from Neutral Beam Injection (NBI), and approximately 3.7 MW from Ion Cyclotron Resonance Heating (ICRH). Pulse 99948 is the best D–T baseline shot in terms of both duration and peak fusion power, which reached 7.8 MW for around 2 s of operation [58].

The PINN reconstruction has been achieved using the diagnostic configuration reported in table 1. The results obtained with this pulse are mostly consistent with the EFIT reconstruction, as shown in figure 13. All the diagnostics used to constrain the equilibrium have been correctly reconstructed, indicating that this discharge was not affected by outliers or anomalous measurements. Regarding the errors in the Grad–Shafranov equation, their distributions are similar. By comparing the EFIT and PINN reconstructed fields, it is evident that the significant differences are concentrated in the core. This is expected since the EFIT used in this paper is the 'magnetic only' version, which uses PUs, SLs, and FLs that

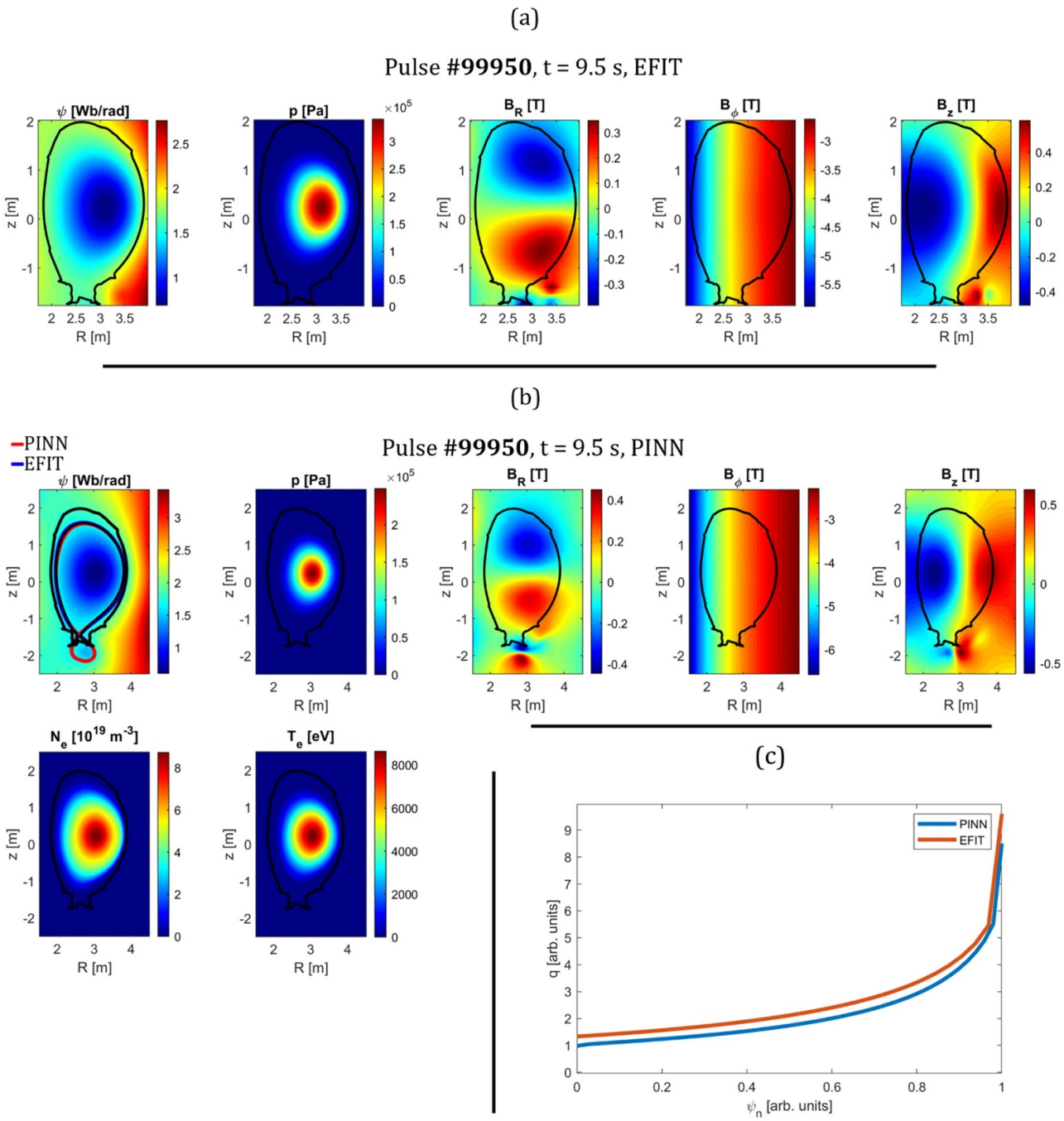

Figure 14. Pulse #99950 ($t = 9.5$ s). EFIT reconstruction (a) vs PINN reconstruction (b) and q profile (c).

constrain the reconstruction only at the boundary, while the core is driven by the Grad–Shafranov equation. However, this is an ill-posed problem. The PINN benefits from the internal constraints (high-resolution TS, interferometer, and polarimeter) and therefore returns a reconstructed equilibrium with the same errors on the Grad–Shafranov equation but with better fits of the internal measurements.

The second high-performance JET pulse is the 99950. This is a hybrid scenario pulse with a toroidal field of 3.45 T, a plasma current of 2.3 MA, and additional heating power of ∼29 MW from NBI and ∼4 MW from ICRH. This pulse made one of the records of DTE2 campaign, with a fusion energy of 45 MJ [10].

The results are shown in figure 14. In this case, as well, the comparison between the measured and reconstructed diagnostics is satisfactory, along with a small error in the Grad–Shafranov equation. The differences between the EFIT and PINN reconstructions are in the core, for the same reasons discussed earlier: the PINN has internal constraints, aiding to reconstruct the core better.

5. Conclusions

In tokamaks, and in general, in all MCNF experimental reactors, a good reconstruction of the equilibrium between the kinetic and magnetic pressures represents an important prerequisite for any plasma study. In this work, a method base on PINN is proposed. The PINN equilibrium reconstruction implements some important features for reliable plasma reconstructions:

- Multi-diagnostics constraints with both local and line-integrated measurements. This allows to include many diagnostics in the model, by allowing a data-integrated equilibrium reconstruction, improving both accuracy and reliability of the outputs.
- High-fidelity physics modelling of the diagnostics. This is fundamental for diagnostics such as polarimeters, where both non-linearities and relativistic effects may be not negligible, as in future tokamaks of the ITER class.
- Direct integration of both magnetic quantities (magnetic flux, magnetic field) and kinetic fields (density and temperature). This is an important advancement with respect to most standard methodologies, such as EFIT, which typically implement a multi-step approach (equilibrium reconstruction with only the magnetic measurements followed by mapping kinetic quantities onto the poloidal magnetic flux).

The model has been deeply investigated. Firstly, systematic analyses have been performed with synthetic cases using TokaLab. The studies have demonstrated the importance of the multi-diagnostics approach and have allowed to quantify the method's performances. In this synthetic case, performances obtained in terms of accuracy report an $R^2 > 99\%$ for all the plasma quantities of interest (magnetic flux, magnetic fields, electronic temperature and electronic density). This is achieved both in absence and in presence of an outlier measurement. The method produces also very reproducible results.

Then, a validation with experimental data has been conducted for pulse 89724 at $t = 15$ s. Firstly, a comparative analysis with respect to EFIT reconstructed fields has been performed. Then a stability analysis and a study of the sensitivity to outliers have been conducted. The validation has been carried out through an ablation test: several reconstructions have been conducted using different sets of diagnostics. For each diagnostic ablated during the PINN training, an analysis of the errors in the reconstruction of the same diagnostic has been conducted: it turns out that the method is able to reconstruct the ablated diagnostic with a Pearson correlation factor always $>97\%$. The evaluations of the R^2 or of the RMSE require some interpretation, since a diagnostic ablation could lead to a volatile problem, such as in the case of the FLs. In such cases, the PINN is indeed capable of reconstructing the field (in this specific case the magnetic flux), but up to a constant. In any case, the capability of reconstructing measurements from diagnostics in agreement with the Grad–Shafranov equation confirms the quality and reliability of the method.

At this point, it is also important to discuss the choice of the adopted PINN architecture. A more Grad–Shafranov-oriented architecture could have been used (see, for example, the Grad–Shafranov Net in [54]), with the property of imposing certain functionalities directly on the architecture as hard constraints, rather than incorporating them into the loss function as soft constraints. However, this work aims to lay the foundation for multi-fluid, time-dependent, and core-edge integrated plasma reconstruction studies. To achieve this, the current work sacrifices some Grad–Shafranov-optimised solutions in favour of flexibility, which will play a fundamental role in future developments. Nevertheless, if one is interested in implementing the Grad–Shafranov within the framework of the present work, it can be accomplished with minor adjustments and modifications.

In terms of physical studies, it is worth mentioning another limitation of the current PINN algorithm, namely the single-fluid approximation. In fact, our PINN algorithm assumes that the electron and ion temperatures and densities are identical. However, this approximation does not apply to these pulses, because they are both externally heated by NBI and ICRH, which results in an ion temperature higher than the electron one. This limitation is expected to be overcome in the next step of the present work, which is the implementation of a multi-fluid approach where ion and electron temperatures are treated separately. It should be noted that this increases the complexity of the inverse problem, which can only be addressed by incorporating additional physical models and/or new diagnostics.

From a practical point of view, the main limitation of the proposed method is the computational speed. Being a trained PINN very specific (since it depends on measurements and since in this case the physical equations rely on the stationary assumption), it is necessary to train it again every time the conditions change (and so for every different measurement and instant of time). Moreover, training a PINN needs significant computational time. For instance, the cases reported in this paper have required approximately between 6 h to a full day on a desktop PC with the following hardware characteristics: 14 cores 13th Gen Intel® Core™ i5-13600KF, 32 GB RAM, 500 GB SSD, and an NVIDIA GeForce GTX 1650 GPU.

However, it is worth noting that:

1. No implementation of parallel computation has been conducted to train our PINNs faster.
2. In the examples reported, we have aimed at high accuracy and have decided to stop the training at a high number of epochs. However, depending on necessities, a different stop condition can be implemented and less iterations could be needed.
3. No pre-trained networks have been used, while specific pretraining could be implemented. This, of course, would speed up the training.

In any case the present versions of the PINNs are not suitable for real-time applications, but they are a valid tool for

post-pulse analysis: the accurate results they can provide, their features as super-resolution and their capability of 'diagnose diagnostics' (filtering out the outlier measurements between data) make them a powerful tool for plasma studies and physical knowledge.

Future perspectives of this work will proceed in different directions:

1. Development of multi-physics multi-diagnostics approaches, by implementing higher-fidelity physics, from the implementation of multi-fluid MHD equations, to take into account differences between ion and electron temperature and density, to the inclusion of a transport model and edge plasma physics. This would lead to a powerful instrument to reconstruct the entire plasma state.
2. Inclusion of uncertainty estimates in the results. Possible approaches could be, for example, methodologies such as Monte Carlo PINN [76], Multi-Output PINN [76], Bayesian PINN [82].
3. Improvement of the PINN architecture. In this work, a standard fully connected architecture has been used, but more sophisticated and efficient solutions (e.g. ResNet) may increase performances.
4. Improvement of convergence schemes, hyper-parameter fine tuning, acceleration by parallelisation and high-performance computing implementation, are also considered to reduce the computational time.

Acknowledgments

This work has been carried out within the framework of the EUROfusion Consortium, funded by the European Union via the Euratom Research and Training Programme (Grant Agreement No. 101052200—EUROfusion). Views and opinions expressed are however those of the author(s) only and do not necessarily reflect those of the European Union or the European Commission. Neither the European Union nor the European Commission can be held responsible for them.

We would like to thank David Terranova for providing us with JET pulses that include validated reconstructed equilibria.

Code and data availability

Synthetic data have been generated using TokaLab, an open-source toolbox: https://github.com/TokaLab.

PINNs code: https://github.com/QEP-Repository/PINN_MHD_Equilibria.

Experimental data are available upon request to the authors and after the permission from EUROfusion consortium.

Conflict of interest

The authors declare no competing interests.

Contribution role (CREDIT)

Novella Rutigliano: Data Curation, Formal Analysis, Investigation, Methodology, Software, Validation, Visualisation, Writing—Original Draft. **Andrea Murari:** Formal Analysis, Methodology, Supervision, Validation, Writing—review & editing. **Pasquale Gaudio:** Methodology, Funding Acquisition, Project Administration, Supervision, Writing—review & editing. **Michela Gelfusa:** Methodology, Funding Acquisition, Project Administration, Supervision, Writing—review & editing. **Riccardo Rossi:** Conceptualization, Formal Analysis, Investigation, Methodology, Supervision, Writing—review & editing.

Appendix A. PINN loss formulation details

In this appendix section, the loss formulation for the PINN is presented in detail. The total loss of the PINN is the weighted sum of the boundary and physics losses:

$$\mathrm{Loss}_{\mathrm{tot}} = \frac{\mathrm{Loss}_{\mathrm{boundaries}} + \alpha \mathrm{Loss}_{\mathrm{physics}}}{1+\alpha} \tag{A1}$$

where the weight α is varied using an adaptive weighting scheme formulated to avoid that the PINN overfits the noise and by ensuring that the physics loss reaches very small error.

The loss of the boundaries evaluates the error between the measurements (y_b) and the 'reconstructed' diagnostics (y_p), i.e. the expected measurements given the PINN predictions. These losses have been formulated with a weighted (w) MSE normalised by the measurement uncertainty (σ_b):

$$\mathrm{Loss}_{\mathrm{boundaries}} = \frac{1}{W_{\mathrm{tot}}} \sum \frac{w(y_p - y_b)^2}{\sigma_b^2} \text{ where } W_{\mathrm{tot}} = \sum w. \tag{A2}$$

Being the measurements affected by noise, the loss of the boundaries should ideally tend to one. However, to both take into account possible non predictable errors in the diagnostics (like offsets and faults) and to ensure a rapid increase of the physics weight, the target is typically set to higher value (from 1.5 to 3). In this work, a target value equal to 1.5 has been used. Details about weighting scheme are in the main text (section 3.2) and in [77]. The formulation of the weighted MSE allows to easily turn off one diagnostic without the need to change the target.

It is now fundamental to describe how each diagnostic boundary loss is defined. In the case of the local measurements, the losses are evaluated as the local predictions against the measurements. For example, for the PUs, the magnetic field seen by each coil is evaluated from the magnetic field reconstructed by the neural network

$$B_{\mathrm{PU_{Rec}},i} = B_R(R_i, z_i)\cos(\gamma_i) + B_z(R_i, z_i)\sin(\gamma_i). \tag{A3}$$

Being R_i and z_i the coordinates of the ith PU centre and γ_i the orientation angle of the pickup coil with respect to the poloidal

surface axis. Then, the loss associated with the PUs is:

$$\mathrm{Loss}_{\mathrm{PU}} = \frac{1}{W_{\mathrm{tot}}} \sum \frac{w_{\mathrm{PU},i} \left(B_{\mathrm{PU},i} - B_{\mathrm{PURec},i}\right)^2}{\sigma^2_{\mathrm{PU}}}. \tag{A4}$$

In the same way, the losses for the FLs, saddle coils, TS and MSE (at the moment implemented on for TokaLab) can be written as:

$$\mathrm{Loss}_{\mathrm{FL}} = \frac{1}{W_{\mathrm{tot}}} \sum \frac{w_{\mathrm{FL},i} \left(\psi_{\mathrm{FL},i} - \psi_{\mathrm{FLRec},i}\right)^2}{\sigma^2_{\mathrm{FL}}}$$

$$\mathrm{Loss}_{\mathrm{SL}} = \frac{1}{W_{\mathrm{tot}}} \sum \frac{w_{\mathrm{SL},i} \left(\Delta\psi_{\mathrm{SL},i} - \Delta\psi_{\mathrm{SLRec},i}\right)^2}{\sigma^2_{\mathrm{SL}}}$$

$$\mathrm{Loss}_{\mathrm{MSE}} = \frac{1}{W_{\mathrm{tot}}} \sum w_{\mathrm{MSE},i} \frac{\left(\theta_{\mathrm{MSE},i} - \theta_{\mathrm{MSERec},i}\right)^2}{\sigma^2_{\mathrm{MSE}}}$$

$$\mathrm{Loss}_{\mathrm{TS}} = \frac{1}{W_{\mathrm{tot}}} \sum \left(\frac{w_{\mathrm{TS},Ne} \left(Ne_{\mathrm{TS},i} - Ne_{\mathrm{TSRec},i}\right)^2}{\sigma^2_{\mathrm{TS},Ne}} + \frac{w_{\mathrm{TS},Te} \left(Te_{\mathrm{TS},i} - Te_{\mathrm{TSRec},i}\right)^2}{\sigma^2_{\mathrm{TS},Te}} \right). \tag{A5}$$

For the line-integrated measurements, the local variables are evaluated on an equally spaced grid of $M = 100$ points for each line. For the interferometer, the LID is reconstructed as follows:

$$\mathrm{LID}_{\mathrm{Rec},i} = \sum_{j=1}^{M} Ne_{\mathrm{Rec},i}\left(R_j, z_j\right) \Delta Z_j \tag{A6}$$

where R_j and z_j are the grid points along the line of sight, ΔZ_j is the step size along the line of sight. Then, the loss is:

$$\mathrm{Loss}_{\mathrm{LID}} = \frac{1}{W_{\mathrm{tot}}} \sum \frac{w_{\mathrm{LID},i} (\mathrm{LID}_i - \mathrm{LID}_{\mathrm{Rec},i})^2}{\sigma^2_{\mathrm{LID}}}. \tag{A7}$$

The plasma polarimetry is implemented using the full Stokes model, and therefore the polarisation evolution is computed with a finite element method based on the explicit backward Euler scheme:

$$\begin{aligned} s_{1,j} &= s_{1,j-1} + \left(\Omega_{2,\mathrm{Rec}}\left(R_j, z_j\right) s_{3,j-1} - \Omega_{3,\mathrm{Rec}}\left(R_j, z_j\right) s_{2,j-1}\right) \Delta Z \\ s_{2,j} &= s_{2,j-1} + \left(\Omega_{3,\mathrm{Rec}}\left(R_j, z_j\right) s_{1,j-1} - \Omega_{1,\mathrm{Rec}}\left(R_j, z_j\right) s_{3,j-1}\right) \Delta Z \\ s_{3,j} &= s_{3,j-1} + \left(\Omega_{1,\mathrm{Rec}}\left(R_j, z_j\right) s_{2,j-1} - \Omega_{2,\mathrm{Rec}}\left(R_j, z_j\right) s_{1,j-1}\right) \Delta Z. \end{aligned} \tag{A8}$$

Both the cold and the hot plasma formulation can be used by modifying $\boldsymbol{\Omega}$ as shown in [55]. Then, the Faraday rotation and Cotton–Mouton phase shift are evaluated from the equations in section 2 and the two losses are:

$$\mathrm{Loss}_{\mathrm{Far}} = \frac{1}{W_{\mathrm{tot}}} \sum \frac{w_{\mathrm{Far},i} (\mathrm{Far}_i - \mathrm{Far}_{\mathrm{Rec},i})^2}{\sigma^2_{\mathrm{Far}}}$$

$$\mathrm{Loss}_{\mathrm{CM}} = \frac{1}{W_{\mathrm{tot}}} \sum \frac{w_{\mathrm{CM},i} (\mathrm{CM}_i - \mathrm{CM}_{\mathrm{Rec},i})^2}{\sigma^2_{\mathrm{CM}}}. \tag{A9}$$

Only for what concerns JET reconstructions there are two other contributions: one is the value of the toroidal magnetic field in absence of plasma at $R_0 = 2.96$ m, called in this paper for brevity F_0, and the other is the constraint on the divertor coil currents.

Concerning F_0, at first its value is evaluated in different points $(R_j,\ z_j)$ where there is not plasma (wall) and then the loss is evaluated as it follows:

$$\begin{aligned} F_{0\mathrm{Rec}} &= B_\phi\left(R_i, z_i\right) R_i \\ \mathrm{Loss}_{F0} &= \frac{1}{W_{\mathrm{tot}}} \sum \frac{w_{F_0,i} \left(F_{0i} - F_{0\mathrm{Rec},i}\right)^2}{\sigma^2_{F_0}} \end{aligned} \tag{A10}$$

where $w_{F_0,i}$ is equal to 1 and $\sigma_{F0} = 0.1184$ mT.

Concerning the reconstruction of the divertor coil currents, let us consider $(R_i,\ z_i)$ with $i = 1{:}\ N$ the discretisation points belonging to the coil C_j with $j = 1{:}4$. Then, the plasma density current and therefore the losses are evaluated as:

$$J_{Cj} = \begin{bmatrix} \frac{1}{N}\sum_{i=1}^{N} J_R(R_i, z_i)_j^{\,2} \\ \frac{1}{N}\sum_{i=1}^{N} J_\phi\left(R_i, z_i\right)_j^{\,2} \\ \frac{1}{N}\sum_{i=1}^{N} J_z(R_i, z_i)_j^{\,2} \end{bmatrix}_j = \begin{bmatrix} J_{RCj} \\ J_{\phi\,Cj} \\ J_{zCj} \end{bmatrix}$$

$$\mathrm{Loss}_{J_{\mathrm{coils}}} = \frac{1}{W_{\mathrm{tot}}} \sum \frac{w_{\mathrm{coils},i}}{\sigma^2_{\mathrm{coils}}} \left[J^2_{R_{Cj}}\Big|_{j=1:4} + J^2_{z_{Cj}}\Big|_{j=1:4} + \left(J^2_{\phi\,Cj}\Big|_{j=1:4} - J_{\phi\,j} \right)^2 \right] \tag{A11}$$

where $w_{\mathrm{coil},i} = 1$ and σ_{coil} is evaluated as the other uncertainties for JET case. Boundaries losses can so be written for TokaLab case as:

$$\begin{aligned} \mathrm{Loss}_{\mathrm{boundaries}} = \mathrm{Loss}_{\mathrm{PU}} + \mathrm{Loss}_{\mathrm{FL}} + \mathrm{Loss}_{\mathrm{SL}} + \mathrm{Loss}_{\mathrm{TS}} + \mathrm{Loss}_{\mathrm{LID}} \\ + \mathrm{Loss}_{\mathrm{Far}} + \mathrm{Loss}_{\mathrm{CM}} + \mathrm{Loss}_{\mathrm{MSE}}. \end{aligned} \tag{A12}$$

And for JET case as:

$$\begin{aligned} \mathrm{Loss}_{\mathrm{boundaries}} = \mathrm{Loss}_{\mathrm{PU}} + \mathrm{Loss}_{\mathrm{FL}} + \mathrm{Loss}_{\mathrm{SL}} + \mathrm{Loss}_{\mathrm{TS}} \\ + \mathrm{Loss}_{\mathrm{LID}} + \mathrm{Loss}_{\mathrm{Far}} + \mathrm{Loss}_{F0} + \mathrm{Loss}_{J\mathrm{coils}}. \end{aligned} \tag{A13}$$

The loss physics is the sum of five terms. The first term aims at minimising the error in fitting the MHD equation. Note that only the pressure balance is needed since both divergence of magnetic field and Ampere's law are automatically fulfilled by the PINN architecture. It is written as:

$$\mathrm{Loss}_{\mathrm{MHD}} = \frac{1}{N_{\mathrm{PhysicalPoints}}} \sum_{i=1}^{N_{\mathrm{PhysicalPoints}}} \frac{f^2_{\mathrm{MHD}}}{C^2_{\mathrm{MHD}}}$$

$$f^2_{\mathrm{MHD}} = \left[\left(J_\phi B_z - J_z B_\phi - \frac{\mathrm{d}p}{\mathrm{d}R} \right)^2 + \left(J_R B_z - J_z B_R \right)^2 + \left(J_R B_\phi - J_\phi B_R - \frac{\mathrm{d}p}{\mathrm{d}z} \right)^2 \right] \cdot i_p$$

$$C_{\mathrm{MHD}} = J_0 B_{p,0} \tag{A14}$$

where i_p is an index equal to 1 if inside the wall and 0 if outside and $N_{\mathrm{PhysicalPoints}}$ is the mini-batch size. For what concerns the normalisation factor, C_{MHD}, $B_{p,0} = B_{t,0} a_0 / (2\pi R_0)$ being $B_{t,0} = F_0/R_0$ where F_0 is the measurement already introduced before, $R_0 = 2.96$ m and $a_0 = 1$ m for JET and $R_0 = 6$ m and $a = 2$ m for TokaLab. Consequently $J_0 = B_{0,p} / (a_0 \mu_0)$. To ensure that current and pressure outside the wall are zero, we introduced the $\mathrm{Loss}_{\mathrm{vacuum}}$:

$$\mathrm{Loss}_{\mathrm{vacuum}} = \frac{1}{N_{\mathrm{PhysicalPoints}}} \sum_{i=1}^{N_{\mathrm{PhysicalPoints}}} \frac{f^2_{\mathrm{vacuum}}}{C^2_{\mathrm{vacuum}}}$$

$$\frac{f^2_{\mathrm{vacuum}}}{C^2_{\mathrm{vacuum}}} = \left[\frac{p_e^2}{p_0^2} (1 - i_p) + \frac{J_R^2}{J_0^2} (1 - i_p) + \frac{{J_\phi}^2}{J_0^2} (1 - i_p)\, i_c + \frac{J_z^2}{J_0^2} (1 - i_p) \right] \tag{A15}$$

where i_c is an index that is equal to 0 inside the divertor coils in the JET case and equal to 1 outside. This allows an independent prediction of the toroidal current inside the divertor coils, limited only by the coils' current measurements through the $\mathrm{Loss}_{J\mathrm{coils}}$. For the TokaLab case, since no divertor coils are present in the model, i_c is always equal to 1. The normalisation factor $p_0 = N_0 T_0$ is: a) for the TokaLab case, $N_0 = 10^{20}\mathrm{m}^{-3}$ and $T_0 = 2 \times 10^4$eV, $p_0 = 321800$ Pa b) for JET, $N_0 = 10^{19}\mathrm{m}^{-3}$ and $T_0 = 10^3$eV, $p_0 = 1609$ Pa. Another physics constraint is that the plasma quantities on the wall are zero:

$$\mathrm{Loss}^2_{\mathrm{borders}} = \frac{1}{N_{\mathrm{borders}}} \sum_{w=1}^{N_{\mathrm{borders}}} \left(\frac{N_e(R_w, z_w)^2}{N_0^2} + \frac{T_e(R_w, z_w)^2}{T_0^2} + \frac{J_R(R_w, z_w)^2}{J_0^2} + \frac{J_\phi(R_w, z_w)^2}{J_0^2} + \frac{J_z(R_w, z_w)^2}{J_0^2} \right). \tag{A16}$$

Being N_{borders} the 100 points, in which the wall has been discretised, $(R_w,\ z_w)$ the coordinates of a point belonging to the wall and the normalisation factors the same already introduced. A soft constraint on the density and temperature gradients has been also implemented. Indeed, the parallel gradient is expected to be very small (typically, magnetic surfaces are considered iso-density and iso-temperature for most calculations), while a much weaker requirement in the orthogonal direction is implemented just to avoid strong fluctuations. However, the orthogonal regularisation actually never plays a role (its contribution is always several order of magnitude smaller than the other loss contributions in the studied cases). The gradients of these quantities can be written:

$$\begin{aligned} (\nabla \cdot N_e)_\perp &= (\nabla \cdot N_e) \cdot \boldsymbol{n} \\ (\nabla \cdot N_e)_\parallel &= (\nabla \cdot N_e) \cdot \boldsymbol{t} \\ (\nabla \cdot T_e)_\perp &= (\nabla \cdot T_e) \cdot \boldsymbol{n} \\ (\nabla \cdot T_e)_\parallel &= (\nabla \cdot T_e) \cdot \boldsymbol{t} \end{aligned} \tag{A17}$$

where $\boldsymbol{t}$ and $\boldsymbol{n}$ are the parallel and orthogonal unit vectors evaluated from the magnetic flux gradient direction:

$$\boldsymbol{n} = \begin{pmatrix} n_R \\ n_z \end{pmatrix} = \begin{pmatrix} \frac{\partial \Psi}{\partial R} \frac{1}{|\Psi|} \\ \frac{\partial \Psi}{\partial z} \frac{1}{|\Psi|} \end{pmatrix}; \boldsymbol{t} = \begin{pmatrix} t_R \\ t_z \end{pmatrix} = \begin{pmatrix} -n_z \\ n_R \end{pmatrix}. \tag{A18}$$

The regularisation term to be minimised can so be defined as:

$$\begin{aligned} \mathrm{Loss}_{\nabla \cdot N_e} &= \frac{1}{N} \sum \left(f^2_{(\nabla \cdot N_e)_\perp} + f^2_{(\nabla \cdot N_e)_\parallel} \right) \\ \mathrm{Loss}_{\nabla \cdot T_e} &= \frac{1}{N} \sum \left(f^2_{(\nabla \cdot T_e)_\perp} + f^2_{(\nabla \cdot T_e)_\parallel} \right) \\ f^2_{(\nabla \cdot N_e)_\perp} &= L^2_\perp \left(\nabla \cdot N_e \right)^2_\perp \\ f^2_{(\nabla \cdot N_e)_\parallel} &= L^2_\parallel \left(\nabla \cdot N_e \right)^2_\parallel \\ f^2_{(\nabla \cdot T_e)_\perp} &= L^2_\perp \left(\nabla \cdot T_e \right)^2_\perp \\ f^2_{(\nabla \cdot T_e)_\parallel} &= L^2_\parallel \left(\nabla \cdot T_e \right)^2_\parallel . \end{aligned} \tag{A19}$$

Being $L_\perp$ and $L_\parallel$ two normalisation lengths equal to $2\pi R_0$ [m] and 10^{-3}[m] respectively. At the end, the whole term quantifying the physical losses can be written as:

$$\begin{aligned} \mathrm{Loss}_{\mathrm{physics}} = \mathrm{Loss}_{\mathrm{MHD}} + \mathrm{Loss}_{\mathrm{vacuum}} + \mathrm{Loss}_{\mathrm{borders}} \\ + \mathrm{Loss}_{\nabla \cdot Ne} + \mathrm{Loss}_{\nabla \cdot Te} \end{aligned} \tag{A20}$$

Appendix B. Losses evolution during training

The weighing of the physics and boundary losses play a crucial role in the convergence and accuracy of PINNs. This work implements an adaptive weighing scheme tailored for noisy boundaries that has proved to have high accuracy and good convergence properties.

In this appendix section, the evolution of the physics, boundary, and total losses are shown in figure B1 for the synthetic, or TokaLab, (a) and JET (b) cases (for pulse #89724). At the beginning, the boundary loss dominates the total loss (α is small) and it is the one that decreases most. When the boundary loss reaches the target value, equal or lower to 1.5, which suggests that the average error between 'reconstructed' diagnostics and measurements are in line with the statistics of the noise, the weight α starts to increase giving more importance to the physics. Therefore, epoch by epoch, the physics equations assume a higher weight, ensuring that the loss boundary is equal or below the target. Such an approach allows reaching very small errors in the physics loss without overfitting the noise.

The adaptive procedure is important because with a fixed weight one could have the following situations:

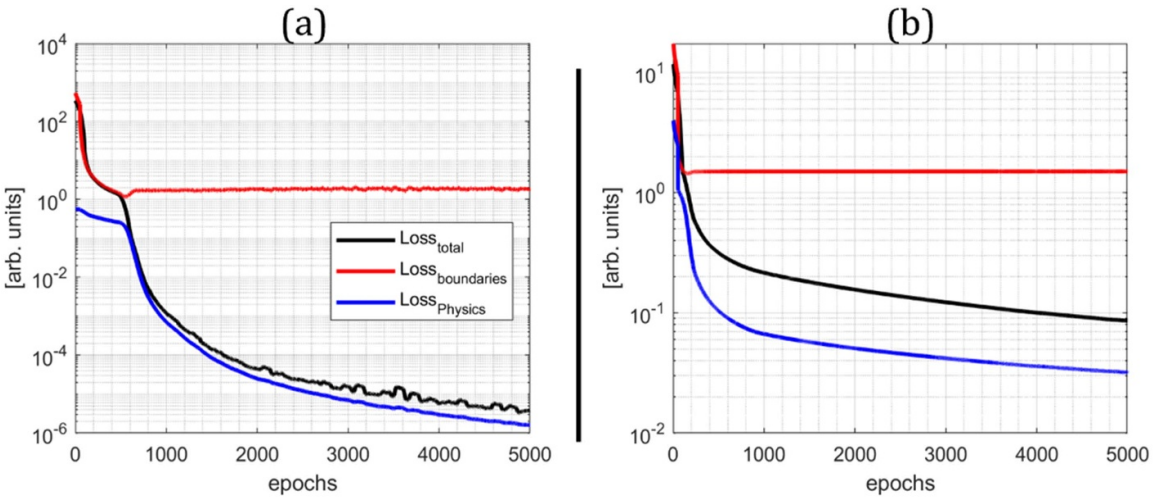

Figure B1. Loss functions trends for (a) the TokaLab reference scenario and (b) JET (pulse #89724) reconstructions with PINNs.

- The weight is too small: the loss physics is never important with respect to the boundary, with result that the PINN overfits the noise and returns a non-physical solution.
- The weight is too large: typically, this has a convergence problem. The boundary loss is negligible and therefore the PINN converges to one of the infinite solutions, in general the trivial solution where all the fields are zero.
- Good weight balance: it allows obtaining a good physical solution in line with the boundaries.

It is important to motivate the reason why the TokaLab case converges to very low physics loss, while JET reconstruction seems to be limited to higher values. This is mostly due to the fact that while TokaLab is simulated, and therefore the synthetic measurements come from a numerical solution of the Grad–Shafranov equation. On the contrary in experimental plasmas there are many aspects that are not solutions of the Grad–Shafranov equation, from small transients induced by the actuators to MHD instabilities (e.g. sawteeth, edge-localised modes).

Appendix C. Complementary details about synthetic results

This appendix section includes some details concerning the synthetic results section, fundamental to render the results reproducible, but not included in the main text to improve readability and maintain the focus on the novelty of the work.

At first, it is important to specify how the TokaLab scenarios are computed. TokaLab equilibria are based on the solution of Grad–Shafranov equation by imposing a specific target separatrix and a relation between the poloidal flux ψ and the toroidal current J_t. By using the separatrix model given in [83], one can simulate equilibria with different upper and low triangularities, elongation, etc. The relation between the toroidal current is a modified version of a standard method [64] which allows to displace the peak

Table C1. TokaLab scenarios parameters (see [83] and [56] for details).

	SN	NT	DN	IQ
Major radius $\boldsymbol{R}_0$ (m)	6	5.9	6	6
Minor radius $\boldsymbol{a}$ (m)	2	1.9	2	2
Vertical position z_0 (m)	0	0.1	0	0
Elongation—upper $\boldsymbol{k}_1$ [arb. units]	1.7	1.7	1.7	1.7
Elongation—bottom $\boldsymbol{k}_2$ [arb. units]	2	2	1.7	2
Triangularity—upper $\boldsymbol{d}_1$ [arb. units]	0.5	−0.5	0.5	0.5
Triangularity—bottom $\boldsymbol{d}_2$ [arb. units]	0.5	−0.5	0.5	0.5
Angle—upper left $\boldsymbol{\gamma}_{\boldsymbol{n},1}$ [rad]	0	0	$\pi/3$	0
Angle—upper right $\boldsymbol{\gamma}_{\boldsymbol{p},1}$ [rad]	0	0	$\pi/6$	0
Angle—bottom left $\gamma_{n,2}$ [rad]	$\pi/3$	$\pi/6$	$\pi/3$	$\pi/3$
Angle—bottom right $\gamma_{p,2}$ [rad]	$\pi/6$	$\pi/3$	$\pi/6$	$\pi/6$
$\boldsymbol{J}_\phi$ parameter 1—$\boldsymbol{\beta}_0$ [1]	0.5	0.5	0.5	0.5
$\boldsymbol{J}_\phi$ parameter 2—$\boldsymbol{\alpha}_1$ [1]	2	2	2	2
$\boldsymbol{J}_\phi$ parameter 3—$\boldsymbol{\alpha}_2$ [1]	2	2	2	2
$\boldsymbol{J}_\phi$ parameter 4—$\boldsymbol{\psi}_{n,\mathbf{peak}}$ [1]	0	0	0	0.3
Plasma current $\boldsymbol{I}_p$ [MA]	12	12	12	15
Toroidal magnetic field $\boldsymbol{B}_\phi$ [T]	5	5	5	5

$$J_{t,\mathrm{profile}}(\psi_n) = \left(\beta_0 \frac{R}{R_0} + \left((1-\beta_0)\frac{R_0}{R}\right)\right)\left(1-\left(\frac{\psi_n - \psi_{n,\mathrm{peak}}}{1-\psi_{n,\mathrm{peak}}}\right)^{\alpha_1}\right)^{\alpha_2}$$
$$J_t = J_{t,\mathrm{profile}} \frac{I_p}{\int J_{t,\mathrm{profile}} \mathrm{d}S}. \tag{C1}$$

Table C1 reports the parameters for the SN, DN, NT and reverse q-profile (IQ) scenario used in this work.

All the simulated (true) and reconstructed quantities and the error fields are reported in figures C1–C3 for the negativity triangularity, the DN and the IQ respectively. Firstly, three different plasma configurations and the reconstructed profiles are shown. Then, a parametric analysis of the magnetic axis reconstruction capability, varying the number of diagnostics in the standard SN configuration, is documented. The reconstructions have been obtained with the full diagnostic set

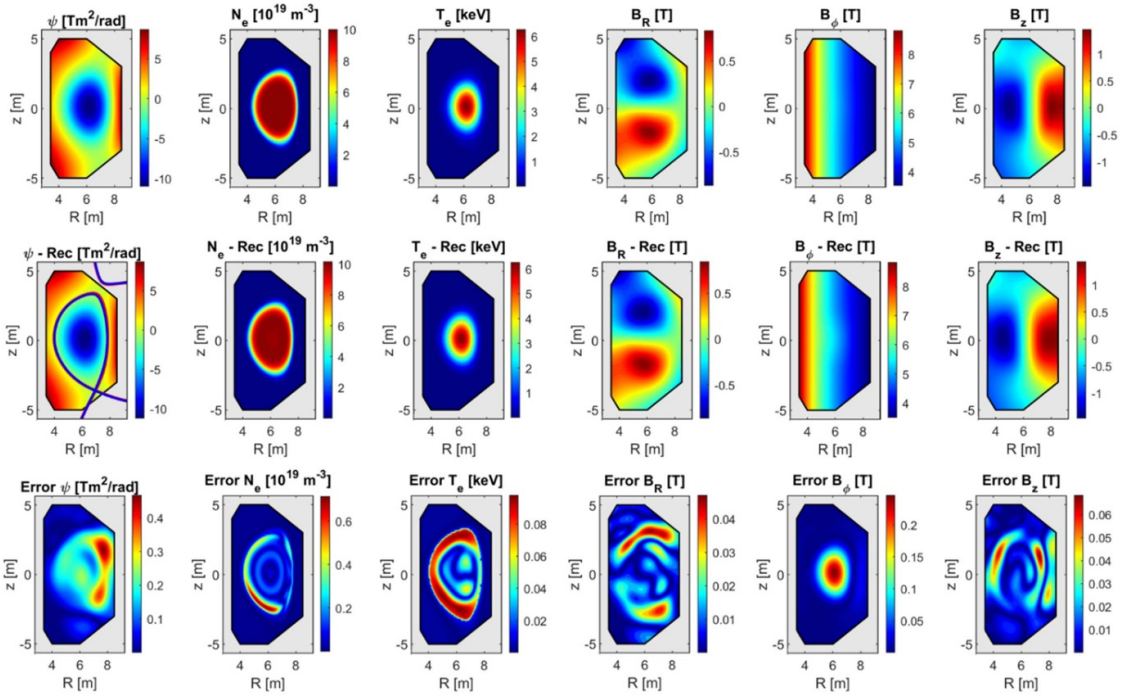

Figure C1. Reconstruction maps for negative triangularity (NT) plasma configuration. Top row: TokaLab scenario. Central row: PINN reconstructed fields. Bottom row: RMSE of the reconstruction.

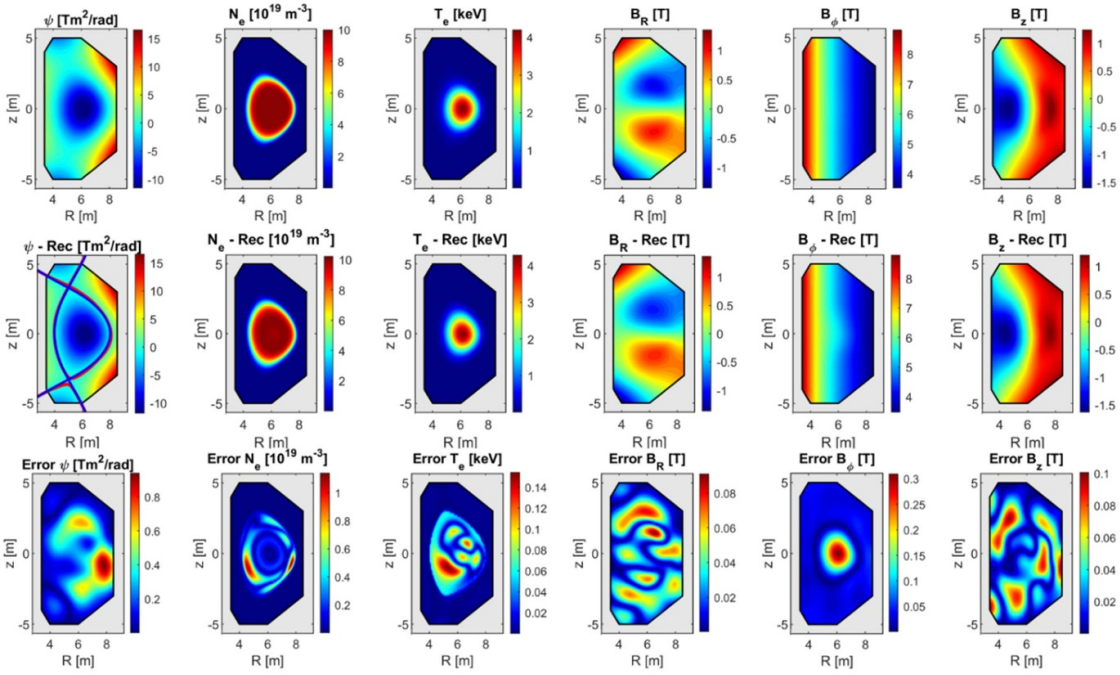

Figure C2. Reconstruction maps for double null (DN) plasma configuration. Top row: TokaLab scenario. Central row: PINN reconstructed fields. Bottom row: RMSE of the reconstruction.

(magnetics, TS, IP, MSE) for TokaLab as described in the main text.

Another typical information relevant for any equilibrium reconstruction problem is the capability to measure the magnetic axis (O-point) and the X-point. This analysis has been performed by varying the set of diagnostics. The two target values are calculated for the TokaLab equilibria and compared with the PINN reconstructed magnetic flux. Being TokaLab equilibria evaluated on a grid a dimension equal to 9 cm along R and 14.3 cm along Z direction, errors below these dimensions are not reliable, or in other words, the true O-point and X-point positions have an uncertainty around half dimension

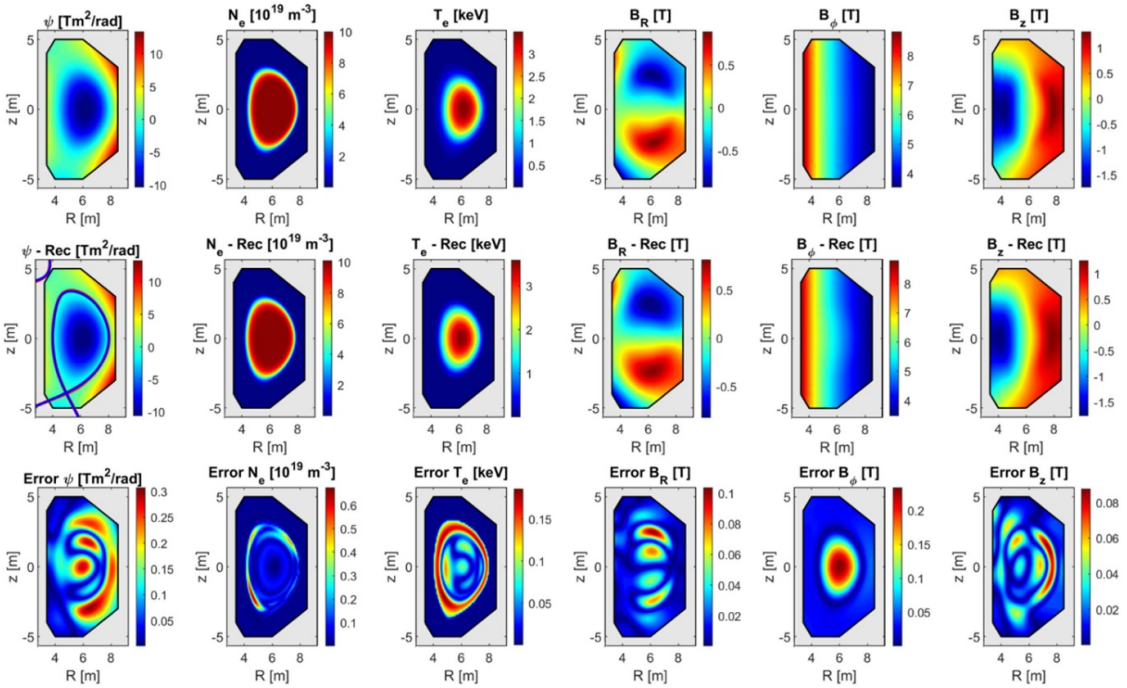

Figure C3. Reconstruction maps for inverted q profile (IQ) plasma configuration. Top row: TokaLab scenario. Central row: PINN reconstructed fields. Bottom row: RMSE of the reconstruction.

Table C2. Error on reconstruction of O point and X point calculated as Euclidean distance.

Diagnostics setting	d_{Opoint} (m)	d_{Xpoint} (m)
Mag + TS	0.1297	0.3392
Mag + TS + INT + POL	0.0751	0.0473
Mag + TS + INT + POL + MSE	0.0751	0.0473

size, i.e. ∼4.5 cm and ∼7.1 cm. To evaluate the error on the position reconstruction of both X point and O point, we evaluated the Euclidean distances (d) between the target points and the reconstructed ones:

$$d_{O\text{point}} = \sqrt{\left(R^{\text{Target}}_{O\text{point}} - R^{\text{Recnstructed}}_{O\text{point}}\right)^2 + \left(Z^{\text{Target}}_{O\text{point}} - Z^{\text{Recnstructed}}_{O\text{point}}\right)^2}$$
$$d_{X\text{point}} = \sqrt{\left(R^{\text{Target}}_{X\text{point}} - R^{\text{Recnstructed}}_{X\text{point}}\right)^2 + \left(Z^{\text{Target}}_{X\text{point}} - Z^{\text{Recnstructed}}_{X\text{point}}\right)^2}. \quad \text{(C2)}$$

Table C2 shows the results, which suggest again that for a small set of diagnostics (magnetics + Thomson scattering), the accuracy is quite limited, while by including interferometer, polarimeter and MSE has beneficial effects on the calculation of these critical points. In these two cases, the errors is of the same order of the grid size and therefore comparison between case 2 and 3 is not statistically significant.

Appendix D. Complementary evaluation of other equilibrium quantities

This appendix reports some complementary evaluations of other equilibrium quantities. At first, both the divergence of magnetic field $\nabla \cdot \boldsymbol{B}$ and plasma density current $\nabla \cdot \boldsymbol{J}$ are evaluated to check the consistency of the physical quantities with physical equations (both are expected to vanish: the former follows directly for the Gauss's law for magnetism, while the latter arises from the definition of the current density given by the second of equation (2)). Second, some integral quantities, namely the thermal and magnetic energy (the latter explained separately in the poloidal and toroidal contributions) are compared with the numerical case TokaLab used as target

$$E_{\text{thermal}} = \int_V \frac{p}{\gamma - 1} \mathrm{d}V = \int_V 2 N_e T_e e \frac{3}{2} \mathrm{d}V$$
$$E_{\text{mag},p} = \int_V \frac{B_p^2}{2\mu_0} \mathrm{d}V$$
$$E_{\text{mag},t} = \int_V \frac{B_t^2}{2\mu_0} \mathrm{d}V \quad \text{(D1)}$$

where $\gamma = \frac{5}{2}$ for a monoatomic plasma and p being the total pressure defined under the assumption of $T_e = T_i$. All the integral quantities are calculated inside the separatrix.

This analysis also provides an opportunity to discuss the advantages of automatic differentiation with respect to numerical differentiation, in particular its independence from the discretisation size of the predictive grid.

Table D1 reports the evaluation of the five analysed quantities for the TokaLab SN scenario, as well as for network predictions obtained on three grids with increasing spatial resolution. The numbers in brackets in the first column represent the discretisation of the prediction grid in the horizontal and vertical dimension respectively.

Table D1. Analysed quantities for TokaLab and for the PINN reconstructions for the three different grid resolutions.

	$\nabla \cdot B\ (\mathrm{Tm}^{-1})$	$\nabla \cdot J\ (\mathrm{A\,m}^{-3})$	$E_{\mathrm{thermal}}\ [J]$	$E_{\mathrm{mag},p}\ [J]$	$E_{\mathrm{mag},t}\ (J)$
TokaLab	3.70×10^{-3}	26.67	1.88×10^{8}	2.68×10^{8}	8.29×10^{9}
Grid_1 [30 × 40]	8.71×10^{-8}	5.37×10^{-2}	1.88×10^{8}	2.77×10^{8}	8.37×10^{9}
Grid_2 [80 × 70]	8.60×10^{-2}	5.25×10^{-2}	1.88×10^{8}	2.74×10^{8}	8.33×10^{9}
Grid_3 [300 × 400]	8.69×10^{-8}	5.16×10^{-2}	1.89×10^{8}	2.74×10^{8}	8.33×10^{9}

The TokaLab equilibrium is a numerical solution of the Grad–Shafranov equation (as discussed in section 2.2) and therefore satisfies both the conditions of $\nabla \cdot B = 0$ and $\nabla \cdot J = 0$. Consequently, the deviations from zero reported in table D1 are solely due to numerical differentiation errors. In this respect, an error of 26 A m^{-3} compared to the reference value of 10^6 A m^{-2} is negligible. Remarkably, the errors obtained with the PINN are four to five orders of magnitude smaller. This improvement is attributed to the reduced differentiation errors associated with automatic differentiation. Moreover, as expected from automatic differentiation, the results exhibit invariance with respect to the grid refinement when automatic differentiation is employed.

ORCID iDs

Novella Rutigliano 0009-0005-4350-4019
Andrea Murari 0000-0002-3932-3865
Pasquale Gaudio 0000-0003-0861-558X
Michela Gelfusa 0000-0001-5158-7292
Riccardo Rossi 0000-0003-4414-6119

References

[1] Donné A.J.H. *et al* 2007 Chapter 7: diagnostics *Nucl. Fusion* **47** S337–84
[2] Hutchinson I.H. 2002 *Principles of Plasma Diagnostics* (Cambridge University Press) (https://doi.org/10.1017/CBO9780511613630)
[3] Orsitto F.P. *et al* 2016 Diagnostics and control for the steady state and pulsed tokamak DEMO *Nucl. Fusion* **56** 026009
[4] Biel W. *et al* 2019 Diagnostics for plasma control—from ITER to DEMO *Fusion Eng. Des.* **146** 465–72
[5] Lovell J., Reinke M.L., Field A.R. and Lomanowski B.A. 2023 Overview and first measurements of the MAST Upgrade bolometer diagnostic *Rev. Sci. Instrum.* **94** 023509
[6] Boboc A., Zabeo L. and Murari A. 2006 Simultaneous Cotton-Mouton and Faraday rotation angle measurements on JET *Rev. Sci. Instrum.* **77**
[7] Boboc A., Gil C., Pastor P., Spuig P., Edlington T. and Dorling S. 2012 Upgrade of the JET far infrared interferometer diagnostic *Rev. Sci. Instrum.* **83** 10E341
[8] Boboc A., Macdonald J., Felton R., Brown M.J., Studholme W. and Cramp S. 2024 JET far-infrared interferometer/polarimeter diagnostic system—40 years of lessons learned *Plasma Phys. Control. Fusion* **66** 085011
[9] Frassinetti L., Beurskens M.N.A., Scannell R., Osborne T.H., Flanagan J., Kempenaars M., Maslov M., Pasqualotto R. and Walsh M. 2012 Spatial resolution of the JET Thomson scattering system *Rev. Sci. Instrum.* **83** 013506
[10] Maslov M., Beurskens M.N.A., Kempenaars M. and Flanagan J. 2013 Status of the JET LIDAR Thomson scattering diagnostic *J. Instrum.* **8** C11009
[11] Mlynar J., Craciunescu T., Ferreira D.R., Carvalho P., Ficker O., Grover O., Imrisek M. and Svoboda J. 2019 Current research into applications of tomography for fusion diagnostics *J. Fusion Energy* **38** 458–66
[12] Fuchs G., Miura Y. and Mori M. 1994 Soft x-ray tomography on tokamaks using flux coordinates *Plasma Phys. Control. Fusion* **36** 307–16
[13] Jardin A., Bielecki J., Mazon D., Peysson Y., Król K., Dworak D. and Scholz M. 2021 Implementing an x-ray tomography method for fusion devices *Eur. Phys. J. Plus* **136** 706
[14] Odstrčil T., Pütterich T., Odstrčil M., Gude A., Igochine V. and Stroth U. 2016 Optimized tomography methods for plasma emissivity reconstruction at the ASDEX Upgrade tokamak *Rev. Sci. Instrum.* **87** 123505
[15] Zharov A., Nemtsev G., Rodionov R. and Kormilitsyn T. 2024 Exploring the potential of machine learning for real-time neutron emissivity tomography using the Vertical Neutron Camera of ITER *Fusion Eng. Des.* **204** 114519
[16] Xing Z.A. *et al* 2021 CAKE: consistent automatic kinetic equilibrium reconstruction *Fusion Eng. Des.* **163** 112163
[17] Li G.Q., Ren Q.L., Qian J.P., Lao L.L., Ding S.Y., Chen Y.J., Liu Z.X., Lu B. and Zang Q. 2013 Kinetic equilibrium reconstruction on EAST tokamak *Plasma Phys. Control. Fusion* **55** 125008
[18] Jiang Y. *et al* 2021 Kinetic equilibrium reconstruction and the impact on stability analysis of KSTAR plasmas *Nucl. Fusion* **61** 116033
[19] Shousha R., Seo J., Erickson K., Xing Z., Kim S., Abbate J. and Kolemen E. 2024 Machine learning-based real-time kinetic profile reconstruction in DIII-D *Nucl. Fusion* **64** 026006
[20] Carpanese F., Felici F., Galperti C., Merle A., Moret J.M. and Sauter O. 2020 First demonstration of real-time kinetic equilibrium reconstruction on TCV by coupling LIUQE and RAPTOR *Nucl. Fusion* **60** 066020
[21] Jinping Q. *et al* 2009 Equilibrium reconstruction in EAST Tokamak *Plasma Sci. Technol.* **11** 142–5
[22] Ren Q., Chu M.S., Lao L.L. and Srinivasan R. 2011 High spatial resolution equilibrium reconstruction *Plasma Phys. Control. Fusion* **53** 095009
[23] Kwak S., Svensson J., Ford O., Appel L. and Ghim Y.-C. (JET Contributors) 2022 Bayesian inference of axisymmetric plasma equilibrium *Nucl. Fusion* **62** 126069
[24] Szepesi G. *et al* 2021 Advanced equilibrium reconstruction for JET with EFIT++ *47th EPS Conf. on Plasma Physics, EPS 2021* pp 633–6
[25] Faugeras B. and Orsitto F. 2018 Equilibrium reconstruction at JET using Stokes model for polarimetry *Nucl. Fusion* **58** 106032
[26] Blum J., Boulbe C. and Faugeras B. 2008 Real-time plasma equilibrium reconstruction in a tokamak *J. Phys.: Conf. Ser.* **135** 012019

[27] Cheng Z., Jiang Y., Zeng L., Gao Z., Tan Y. and Wang S. 2025 Equilibrium reconstruction in the Sino-United spherical tokamak *Fusion Eng. Des.* **213** 114871
[28] Lao L.L. *et al* 2022 Application of machine learning and artificial intelligence to extend EFIT equilibrium reconstruction *Plasma Phys. Control. Fusion* **64** 074001
[29] Murari A., Mazon D., Gelfusa M., Folschette M. and Quilichini T. 2011 Residual analysis of the equilibrium reconstruction quality on JET *Nucl. Fusion* **51** 053012
[30] Lao L.L., John H.S., Stambaugh R.D., Kellman A.G. and Pfeiffer W. 1985 Reconstruction of current profile parameters and plasma shapes in tokamaks *Nucl. Fusion* **25** 1611–22
[31] Mitrishkin Y.V., Korenev P.S., Konkov A.E., Kruzhkov V.I. and Ovsiannikov N.E. 2021 New identification approach and methods for plasma equilibrium reconstruction in D-shaped tokamaks *Mathematics* **10** 40
[32] Anand H. *et al* 2024 Real-time plasma equilibrium reconstruction and shape control for the MAST Upgrade tokamak *Nucl. Fusion* **64** 086051
[33] Anand H., Coda S., Felici F., Galperti C. and Moret J.-M. 2017 A novel plasma position and shape controller for advanced configuration development on the TCV tokamak *Nucl. Fusion* **57** 126026
[34] Ostuni V., Artaud J.F., Giruzzi G., Joffrin E., Heumann H. and Urano H. 2021 Tokamak discharge simulation coupling free-boundary equilibrium and plasma model with application to JT-60SA *Nucl. Fusion* **61** 026021
[35] Yue X.N., Xiao B.J., Luo Z.P. and Guo Y. 2013 Fast equilibrium reconstruction for tokamak discharge control based on GPU *Plasma Phys. Control. Fusion* **55** 085016
[36] Bergmann M., Fischer R., Angioni C., Höfler K., Molina Cabrera P., Görler T., Luda T., Bilato R., Tardini G. and Jenko F. 2024 Plasma profile reconstruction supported by kinetic modeling *Nucl. Fusion* **64** 056024
[37] Shafranov V.D. 1966 Plasma equilibrium in a magnetic field *Rev. Plasma Phys.* **2** 103
[38] Giannone L. *et al* 2024 Magnetics only real-time equilibrium reconstruction on ASDEX Upgrade *Plasma Phys. Control. Fusion* **66** 045017
[39] Qian Z.H. *et al* 2024 Equilibrium reconstruction constrained by the consistency of current simulation on EAST *Nucl. Fusion* **64** 056028
[40] Sun X., Akçay C., Bechtel Amara T., Kruger S.E., Lao L.L., Liu Y., Madireddy S. and McClenaghan J. 2024 Impact of various DIII-D diagnostics on the accuracy of neural network surrogates for kinetic EFIT reconstructions *Nucl. Fusion* **64** 086065
[41] Rossi R., Orsitto F.P., Spolladore L., Wyss I. and Gaudio P. 2020 On the interpretability and uncertainty propagation of polarimetric measurements in thermonuclear plasmas as a function of the input polarisation and laser wavelength *Plasma Phys. Control. Fusion* **62** 105019
[42] Wu H., Wang T., Jardin A., Mazon D., Verdoolaege G. and The West T. 2025 Bayesian integrated estimation of two-dimensional tungsten concentration profiles at WEST using soft x-ray and bolometry diagnostics *Plasma Phys. Control. Fusion* **67** 085001
[43] Wang T., Mazon D., Svensson J., Liu A., Zhou C., Xu L., Hu L., Duan Y. and Verdoolaege G. 2019 Bayesian data analysis for Gaussian process tomography *J. Fusion Energy* **38** 445–57
[44] Dinklage A. *et al* 2008 Integrated data analysis for fusion: a Bayesian tutorial for fusion diagnosticians *AIP Conf. Proc.* **988** 471–80
[45] Raissi M., Perdikaris P. and Karniadakis G.E. 2019 Physics-informed neural networks: a deep learning framework for solving forward and inverse problems involving nonlinear partial differential equations *J. Comput. Phys.* **378** 686–707
[46] Karniadakis G.E., Kevrekidis I.G., Lu L., Perdikaris P., Wang S. and Yang L. 2021 *Physics-Informed Machine Learning* (Springer) (https://doi.org/10.1038/s42254-021-00314-5)
[47] Cuomo S., Di Cola V.S., Giampaolo F., Rozza G., Raissi M. and Piccialli F. 2022 Scientific machine learning through physics–informed neural networks: where we are and what's next *J. Sci. Comput.* **92** 88
[48] Kumar J., Zarzoso D., Grandgirard V., Ebert J. and Kesselheim S. 2023 Physics informed neural networks applied to the description of wave-particle resonance in kinetic simulations of fusion plasmas (arXiv:2308.12312)
[49] Rahman H.U., Hussain A., Ilyas M., Ahmed M. and Rehman H. 2025 A multi-domain physics-informed neural network for transient thermal analysis of a tokamak divertor *Fusion Eng. Des.* **216** 115036
[50] Zhao C., Zhang F., Lou W., Wang X. and Yang J. 2024 A comprehensive review of advances in physics-informed neural networks and their applications in complex fluid dynamics *Phys. Fluids* **36** 101301
[51] Fan D., Xu Y., Wang H. and Wang J. 2023 Comparative assessment for pressure field reconstruction based on physics-informed neural network *Phys. Fluids* **35** 077116
[52] Rossi R., Murari A., Craciunescu T., Wyss I., Mazon D., Pau A., Costantini A. and Gelfusa M. 2025 Time-resolved, physics-informed neural networks for tokamak total emission reconstruction and modelling *Nucl. Fusion* **65** 036030
[53] Wyss I., Murari A., Peluso E., Gelfusa M., Gaudio P. and Rossi R. 2024 On the accuracy of a fast time resolution inversion method for the detection of different radiation patterns in fusion reactors *Fusion Eng. Des.* **205** 114527
[54] Rossi R., Gelfusa M. and Murari A. 2023 On the potential of physics-informed neural networks to solve inverse problems in tokamaks *Nucl. Fusion* **63** 126059
[55] Rutigliano N., Rossi R., Murari A., Gelfusa M., Craciunescu T., Mazon D. and Gaudio P. 2025 Physics-informed neural networks for the modelling of interferometer-polarimetry in tokamak multi-diagnostic equilibrium reconstructions *Plasma Phys. Control. Fusion* **67** 065029
[56] TokaLab 2026 TokaLab: a Virtual Tokamak for Education and Research (available at: https://tokalab.github.io/) (Accessed 7 August 2025)
[57] Maggi C.F. *et al* 2019 Isotope identity experiments in JET-ILW with H and D L-mode plasmas *Nucl. Fusion* **59** 076028
[58] Garzotti L. *et al* 2025 Development of high-current baseline scenario for high deuterium–tritium fusion performance at JET *Plasma Phys. Control. Fusion* **67** 075011
[59] Maggi C.F. *et al* 2024 Overview of T and D–T results in JET with ITER-like wall *Nucl. Fusion* **64** 112012
[60] Maslov M. *et al* 2023 JET D-T scenario with optimized non-thermal fusion *Nucl. Fusion* **63** 112002
[61] Brix M., Hawkes N.C., Boboc A., Drozdov V. and Sharapov S.E. 2008 Accuracy of EFIT equilibrium reconstruction with internal diagnostic information at JET *Rev. Sci. Instrum.* **79** 10F325
[62] O'Brien D.P., Lao L.L., Solano E.R., Garribba M., Taylor T.S., Cordey J.G. and Ellis J.J. 1992 Equilibrium analysis of iron core tokamaks using a full domain method *Nucl. Fusion* **32** 1351–60
[63] Grad H. and Rubin H. 1958 Hydromagnetic equilibria and force-free fields *J. Nucl. Energy* **7** 284–5
[64] Coleman M. and McIntosh S. 2020 The design and optimisation of tokamak poloidal field systems in the BLUEPRINT framework *Fusion Eng. Des.* **154** 111544
[65] Wesson J. 2011 *Tokamaks* (Oxford University Press)

[66] Segre S.E. 1999 A review of plasma polarimetry—theory and methods *Plasma Phys. Control. Fusion* **41** R57–R100
[67] Kim D. and Lee J. 2024 A review of physics informed neural networks for multiscale analysis and inverse problems *Multiscal. Sci. Eng.* **6** 1–11
[68] Thanasutives P., Morita T., Numao M. and Fukui K. 2023 Noise-aware physics-informed machine learning for robust PDE discovery *Mach. Learn. Sci. Technol.* **4** 015009
[69] Baydin A.G., Pearlmutter B.A., Radul A.A. and Siskind J.M. 2015 Automatic differentiation in machine learning: a survey
[70] Zhu Y., Zabaras N., Koutsourelakis P.-S. and Perdikaris P. 2019 Physics-constrained deep learning for high-dimensional surrogate modeling and uncertainty quantification without labeled data *J. Comput. Phys.* **394** 56–81
[71] Sobol' I.M., Asotsky D., Kreinin A. and Kucherenko S. 2011 Construction and comparison of high-dimensional Sobol' generators *Wilmott* **2011** 64–79
[72] Sobol' I.M. 1967 On the distribution of points in a cube and the approximate evaluation of integrals *USSR Comput. Math. Math. Phys.* **7** 86–112
[73] Kingma P.D. and Ba J. 2015 Adam: a method for stochastic optimization *3rd Int. Conf. for Learning Representations* (*San Diego*, *7–9May 2015*)
[74] Rohrhofer F.M., Posch S., Gobnitzer C. and Geiger B.C. 2023 Data vs. physics: the apparent Pareto front of physics-informed neural networks *IEEE Access* **11** 86252–61
[75] Xiang Z., Peng W., Liu X. and Yao W. 2022 Self-adaptive loss balanced physics-informed neural networks *Neurocomputing* **496** 11–34
[76] Yang M. and Foster J.T. 2022 Multi-output physics-informed neural networks for forward and inverse PDE problems with uncertainties *Comput. Methods Appl. Mech. Eng.* **402** 115041
[77] Rutigliano N., Rossi R. and Gaudio P. 2026 A novel adaptive weighting scheme for physics-informed neural networks in presence of noisy data and outliers *engineering research express Eng. Res. Express* **8** 045217
[78] Mirnov V.V., Ding W.X., Brower D.L., Van Zeeland M.A. and Carlstrom T.N. 2007 Finite electron temperature effects on interferometric and polarimetric measurements in fusion plasmas *Phys. Plasmas* **14** 102105
[79] Gelfusa M. *et al* 2013 Influence of plasma diagnostics and constraints on the quality of equilibrium reconstructions on Joint European Torus *Rev. Sci. Instrum.* **84** 103508
[80] Gao H., Sun L. and Wang J.-X. 2021 Super-resolution and denoising of fluid flow using physics-informed convolutional neural networks without high-resolution labels *Phys. Fluids* **33** 073603
[81] Sautory T. and Shadden S.C. 2024 Unsupervised denoising and super-resolution of vascular flow data by physics-informed machine learning *J. Biomech. Eng.* **146** 091006
[82] Yang L., Meng X. and Karniadakis G.E. 2021 B-PINNs: Bayesian physics-informed neural networks for forward and inverse PDE problems with noisy data *J. Comput. Phys.* **425** 109913
[83] Jean J. 2011 HELIOS: a zero-dimensional tool for next step and reactor studies *Fusion Sci. Technol.* **59** 308–49